Seasonal variability of the Canary Current: A numerical study

Evan Mason,[1,2] Francois Colas,[3] Jeroen Molemaker,[3] Alexander F. Shchepetkin,[3] Charles Troupin,[4] James C. McWilliams,[3] and Pablo Sangrà[2]

[1]   A high-resolution numerical model study of the Canary Basin in the northeast subtropical Atlantic Ocean is presented. A long-term climatological solution from the Regional Oceanic Modeling System (ROMS) reveals mesoscale variability associated with the Azores and Canary Current systems, the northwest African coastal upwelling, and the Canary Island archipelago. The primary result concerns the Canary Current (CanC) which, in the solution, transports ~3 Sv southward in line with observations. The simulated CanC has a well-defined path with pronounced seasonal variability. This variability is shown to be mediated by the westward passage of two large annually excited counterrotating anomalous structures that originate at the African coast. The anomalies have a sea surface expression, permitting their validation using altimetry and travel at the phase speed of baroclinic planetary (Rossby) waves. The role of nearshore wind stress curl variability as a generating mechanism for the anomalies is confirmed through a sensitivity experiment forced by low-resolution winds. The resulting circulation is weak in comparison to the base run, but the propagating anomalies are still discernible, so we cannot discount a further role in their generation being played by annual reversals of the large-scale boundary flow that are known to occur along the African margin. An additional sensitivity experiment, where the Azores Current is removed by closing the Strait of Gibraltar presents the same anomalies and CanC behavior as the base run, suggesting that the CanC is rather insensitive to upstream variability from the Azores Current.

Citation: Mason, E., F. Colas, J. Molemaker, A. F. Shchepetkin, C. Troupin, J. C. McWilliams, and P. Sangrà (2011), Seasonal variability of the Canary Current: A numerical study, *J. Geophys. Res.*, *116*, C06001, doi:10.1029/2010JC006665.

1. Introduction

[2]   Motivated by interest in the seasonal variability of the dynamics and processes in the eastern boundary of the North Atlantic Subtropical Gyre (NASG), a climatology-forced quasi-equilibrium numerical model configuration has been developed using the Regional Oceanic Modeling System (ROMS) [*Shchepetkin and McWilliams*, 2005, 2009]. The model is configured with a domain (outlined in red in Figure 1) spanning the Canary Basin at a mesoscale resolution of 7.5 km, and is integrated for 50 years. The long solution permits a robust evaluation to be made of the seasonal cycle and variability in this region. Our focus in this paper is on the seasonality of the Canary Current (CanC) north of the Canary Island archipelago. The CanC has been frequently observed but has not yet been the subject of a high-resolution climatological numerical study. An impor-

tant open question concerns the path of the CanC. While a broad seasonal cycle has been identified, questions remain about variability in the path of the current, and its interaction with the coastal upwelling region. We comment also on the importance of the Azores Current (AzC) as a source for the CanC in the light of results from an additional simulation where the AzC is removed by closing the Strait of Gibraltar.

[3]   The paper is organized as follows. Sections 2 and 3 briefly reviews our current knowledge of the physical oceanography of the study region. In section 4 we describe the ROMS model configuration and the methodologies developed in realizing the present solution. Section 5 presents a validation of the model solution through comparison with observations. This solution is presently in use as a parent solution to force the boundaries of several higher-resolution nested regional configurations within the Canary Basin; the validation serves to underpin these future studies as well as the results presented in this paper. Section 6 addresses the central question concerning the CanC analysis identified above. Results from two sensitivity experiments are presented in section 7. Finally, we make some brief conclusions in section 8.

2. The Canary Current System

[4]   The Canary Current System (CCS) lies within the Canary Basin, whose limits are loosely defined between 10°

[1]Departament d'Oceanografía Física, Institut de Ciències del Mar, CMIMA-CSIC, Barcelona, Spain.
[2]Departamento de Física, Universidad de Las Palmas de Gran Canaria, Las Palmas de Gran Canaria, Spain.
[3]Institute of Geophysics and Planetary Physics, University of California, Los Angeles, California, USA.
[4]GeoHydrodynamics and Environment Research, Universitè de Liège, Liège, Belgium.
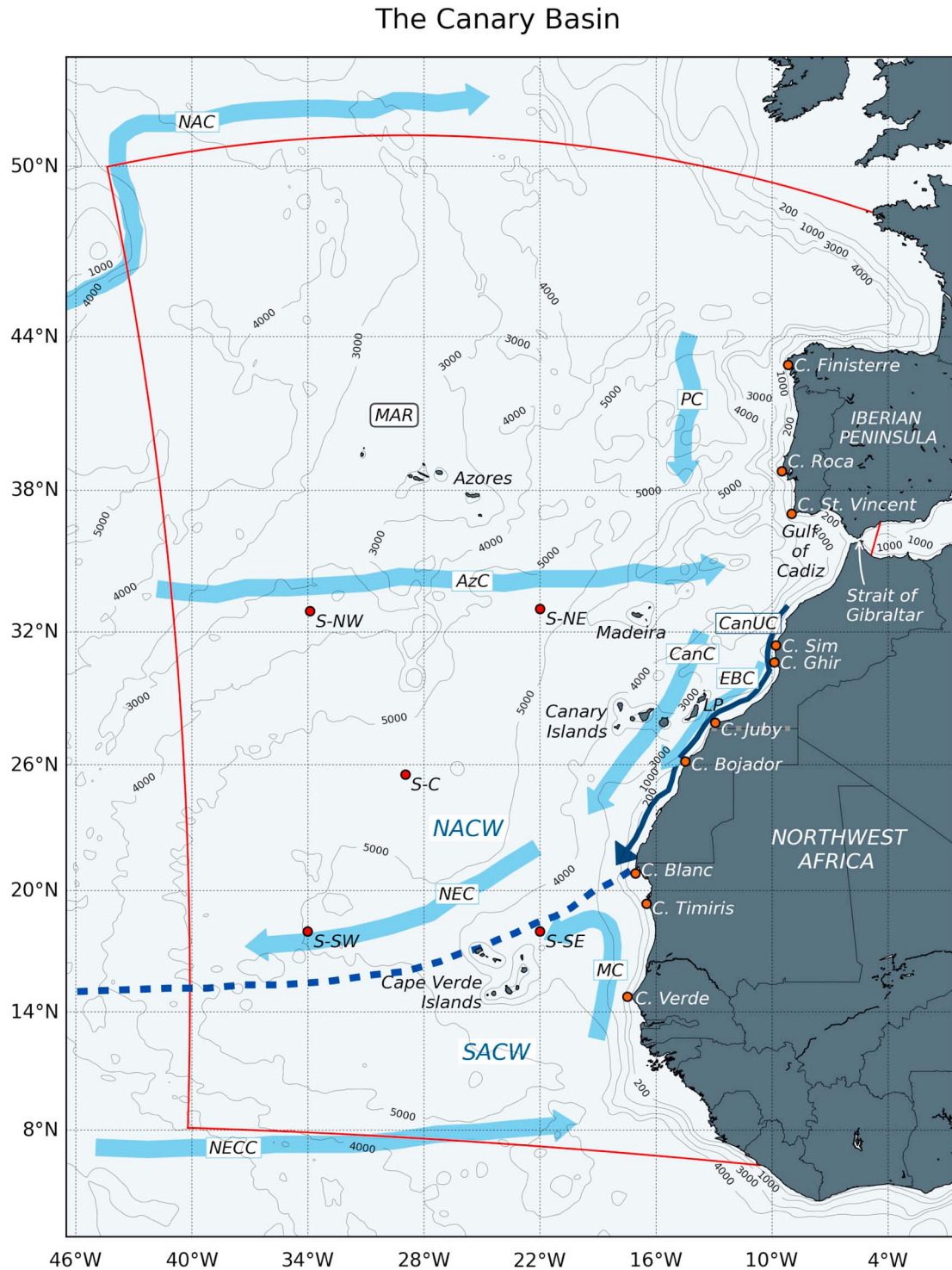
The Canary Basin

Figure 1. Topology and schematic surface circulation of the Canary Basin in the subtropical northeast Atlantic. The boundary of the L0 model domain is outlined in red. Red circles show the positions of moorings used in the text (see section 5.1 and Table 1). AzC, Azores Current; CanC, Canary Current; CanUC, Canary Upwelling Current; EBC, Eastern Boundary Current (see section 3); MC, Mauritania Current; NEC, North Equatorial Current; NECC, North Equatorial Countercurrent; PC, Portugal Current; MAR, Mid-Atlantic Ridge; LP, Lanzarote Passage. Dark blue dashed line marks the position of the Cape Verde Frontal Zone. Contours in black mark isobaths at 200, 1000, 3000, 4000, and 5000 m.

and 40°N in the northeast Atlantic Ocean [*Spall*, 1990; *Arhan et al.*, 1994; *Aristegui et al.*, 2006]. Figure 1 presents a schematic diagram of the large-scale current structure, and a key to the main geographic and bathymetric features. At the Gulf of Cadiz in the north, the Strait of Gibraltar facilitates exchange between the North Atlantic and the Mediterranean Sea. Several island groupings populate the region, including the Canary Island archipelago near to Cape Juby (~28.5°N), and Madeira which lies in deep waters ~800 km offshore of Cape Sim (~31.4°N).

[5] The CCS, composed of the Canary Current and the Canary Upwelling Current (CanUC), is one of the four main upwelling regions of the world ocean and therefore supports an important fishery [*Arístegui et al.*, 2009]. The northeasterly alongshore Trade wind regime drives a near-permanent upwelling of relatively cool North Atlantic Central Water (NACW) into the euphotic zone [*Lathuiliére et al.*, 2008]. The winds, which reach their peak in summer, are modulated by the seasonal migration of the Azores high-pressure cell [*Wooster et al.*, 1976; *Mittelstaedt*, 1991]. Connectivity in the CCS between the open ocean and the coastal upwelling is uniquely enhanced by the Canary Islands, whose presence just off the northwest African coast perturbs both the atmospheric and oceanic flow [*Arístegui et al.*, 1994; *Barton et al.*, 1998; *Brochier et al.*, 2011].

[6] The CanC constitutes the eastern boundary current of the NASG and, as such, has generally been viewed as a broad weak flow spanning the transition zone between the open ocean and the coastal region. The current transports ~3 Sv southwestward, parallel to the African coast, and occupies much of the central water layer (~0–700 m) [*Stramma*, 1984; *Stramma and Siedler*, 1988; *Navarro-Pérez and Barton*, 2001; *Fraile-Nuez and Hernández-Guerra*, 2006; *Machín et al.*, 2006]. Originating in the region between Madeira and the African coast, the CanC is seen as a natural extension of the zonal AzC as it approaches the eastern boundary [*Stramma*, 1984]. *Stramma and Siedler* [1988] showed that the current demonstrates seasonal dependence, it tends to be found far offshore near to Madeira in winter while in summer it strengthens and occupies a more central position between Madeira and the African coast. After passing the Canary Islands, the CanC feeds into the North Equatorial Current (NEC) north of the Cape Verde Frontal Zone (CVFZ) [*Barton*, 1987; *Zenk et al.*, 1991; *Hernández-Guerra et al.*, 2005].

[7] Recent studies suggest that the CanC north of the Canary Islands has a better defined pathway than has previously been recognized [*Zhou et al.*, 2000; *Pelegrí et al.*, 2005a; *Machín et al.*, 2006]. In a series of seasonal meridional geostrophic velocity sections at 32°N in 1997 and 1998, *Machín et al.* [2006] observed the CanC to be a relatively strong (>0.08 m s^{-1}) ~800 m deep current closely centered around 14°W in summer. *Pelegrí et al.* [2005a] stress close interconnectivity between the open ocean CanC and the coastal upwelling region: The CanUC, the nearshore equatorward surface jet associated with the upwelling [*Pelegrí et al.*, 2006], is present for most of the year over the northwest African shelf. In late autumn, the portion of the CanUC near to the Canary archipelago reverses and, in the vicinity of Cape Ghir, detaches from the coast and moves offshore. *Pelegrí et al.* [2005a] speculate that this leads to the formation of a large wintertime cyclonic

circulation cell that extends around the archipelago. Cyclonic flow around the Canary Islands would imply a large-scale poleward flow at the eastern boundary (i.e., within the ~1300 m deep Lanzarote Passage (LP) that separates the easternmost of the Canary Islands from the African continent; Figure 1), yet the mean flow here is equatorward. However, there is observational evidence for periodic (typically autumn) poleward flows in the upper levels of the LP [*Hernández-Guerra et al.*, 2002; *Knoll et al.*, 2002; *Machín and Pelegrí*, 2009; *Fraile-Nuez et al.*, 2010; *Machín et al.*, 2010] (lending support to *Pelegrí et al.*'s [2005a] suggestion of a cyclonic loop). As we shall show in sections 6 and 7 these reversals at the eastern boundary may play an important role in the variability of the CanC, and so a brief description of this boundary flow is warranted.

3. Variability in the Lanzarote Passage

[8] The flow through the LP is generally considered to be a part of the CanC. However, owing to its location between the Canary Islands and the African boundary, its dynamics may be expected to differ from the open ocean CanC. It is also important to note that, given its dimensions, it can be considered a large-scale flow, and should not be confused with the CanUC that is found along the African slope and shelf. The flow spans over half the breadth of the LP (~90 km), and contains three water masses: a central water layer composed of NACW (~0–600 m), and an intermediate layer with both Antarctic Intermediate Water (AAIW; ~600–1100 m) and Mediterranean Water (MW; ~900 m to the bottom). The LP is a conduit for the northward penetration of AAIW along the African boundary, which has been observed beyond the passage to as far north as 33°N in autumn [*Machín and Pelegrí*, 2009].

[9] Some authors [e.g., *Fraile-Nuez et al.*, 2010] have referred to the LP flow as the Eastern Boundary Current (EBC; use of capitals distinguishes it from the generic *eastern boundary current*) and we herein adopt this term to differentiate it from the CanC and the CanUC. In addition, where appropriate we use the notation EBC$_{NACW}$ and EBC$_{AAIW}$ to refer to the passage flow within the respective water layers.

[10] The mean EBC$_{NACW}$ and EBC$_{AAIW}$ flows are equatorward and poleward, respectively. This is confirmed by a 9 year time series of current meter data from a mooring within the LP that shows a close inverse relationship between the transports in the two layers, suggesting that they may be strongly coupled [*Fraile-Nuez et al.*, 2010]. The current meters also clearly show brief reversals in the mean flow in both layers that take place around November. *Machín and Pelegrí* [2009] and *Machín et al.* [2010] focus on the AAIW layer and propose that remote forcing related to potential vorticity conservation in the eastern tropical Atlantic drives the EBC$_{AAIW}$ reversals. The poleward extent of the EBC$_{NACW}$ reversal is not reported, but *Machín et al.* [2006] observed a 0.5 Sv poleward flow over the NACW layer near the coast at 32°N in January 1997, indicating that it may round Cape Ghir.

[11] The CCS is therefore a complex region, composed of a number of distinct currents and countercurrents, that are driven by both local and remote forcing. Yet despite the efforts outlined above, uncertainty remains about the posi-

Table 1. Description of Observational Data Products Used in the Forcing and/or Validation of the L0 Solution

Product	Description
AVISO	18 years (October 1992 to November 2009) of mean absolute dynamic topography, computed by Archiving, Validation and Interpretation of Satellite Oceanographic data using weekly merged altimeter data and the Rio05 mean dynamic topography [*Rio and Hernández*, 2004; *Pascual et al.*, 2006].
NCEP	10 m monthly mean wind speeds from the Reanalysis Project 1 [*Kalnay et al.*, 1996] at National Centers for Environmental Prediction (NCEP) for the period September 1999 to August 2007.
OSTIA	Global high-resolution (6 km) SST from the Operational Sea Surface Temperature and Sea Ice Analysis (OSTIA) [*Stark et al.*, 2007]. Records are daily, beginning in April 2006.
Pathfinder	Monthly climatology of 9.28 km global SST from the NOAA/NASA AVHRR Oceans Pathfinder Program (version 4) [*Kilpatrick et al.*, 2001].
SCOW	8 year (September 1999 to August 2007) QuikSCAT monthly wind stress climatology, the Scatterometer Climatology of Ocean Winds by *Risien and Chelton* [2008].
Subduction Experiment	Five moorings (labeled NW, NE, C, SW, SE in Figure 1) measuring currents and temperature over the water column, deployed as part of the Subduction Experiment in the northeast Atlantic Between June 1991 and June 1993 [*Weller et al.*, 2004].
SVP	The Surface Velocity Program (SVP) monthly drifter-derived climatology of surface currents at 1° resolution (data up to 31 March 2009), described by *Lumpkin and Garraffo* [2005]. The drifters are drogued at 15 m.

tion of the CanC and its seasonal dependence, and the mechanism(s) which govern its variability.

4. The ROMS Model

[12] Following the examples of the ROMS U.S. West Coast and Peru upwelling quasi-equilibrium model simulations of *Marchesiello et al.* [2003] and *Penven et al.* [2005], respectively, we base our model on a monthly climatological forcing cycle. This approach, where synoptic and interannual forcing is excluded, reveals the intrinsic variability that occurs at smaller scales within a regional system, while capturing basin-scale structures that are determined by low-frequency atmospheric forcing at the surface and also transmitted through the open model boundaries.

[13] ROMS is a free surface primitive equation curvilinear coordinate ocean model, where the barotropic and baroclinic momentum equations are resolved separately. ROMS uses a terrain-following (or *sigma*) vertical coordinate system. We use the UCLA version of the ROMS code which features a modification to the commonly used Flather-type [*Flather*, 1976] barotropic open boundary condition that improves the solution behavior near the open boundaries (for the modifications see *Mason et al.* [2010]), and a new sigma coordinate transformation that helps mitigate pressure gradient errors [*Shchepetkin and McWilliams*, 2009]. Subgrid-scale vertical mixing processes are parameterized using the nonlocal K profile planetary (KPP) boundary layer formulation of *Large et al.* [1994]. ROMS features weakly diffusive advection schemes making it a preferred choice for high-resolution simulations where small-scale processes become important.

4.1. Model Domain and Configuration

[14] The ocean model experiments were conducted using a $442 \times 646 \times 32$ grid covering the northeast Atlantic (~1°–45°W, ~6°–51°N; 3300×4830 km²). All four model boundaries are open. Increased near-surface resolution is achieved using a surface stretching factor $\theta_s = 6$, while at

the bottom $\theta_b = 0$. The sigma coordinate system is a new formulation that ensures good resolution of the thermocline independently of the total depth, h [*Shchepetkin and McWilliams*, 2009].

[15] A prime requirement for a valid solution are correct levels of mesoscale variability for the AzC [*Smith et al.*, 2000]. We therefore (1) leave the Strait of Gibraltar open and parameterize the flux of MW into the domain as detailed in section 4.3 (see also section 7.1) and (2) use a small sponge $\nu_{max} = 25$ m² s^{-1} along the open boundaries in order not to suppress variability generated at the open western boundary where the AzC enters the domain. (Early experiments with a 15 km grid using sponge values of $\gg 25$ m² s^{-1} were unsatisfactory because the high sea surface height variance west of the Mid-Atlantic Ridge seen in Figure 6c, which is associated with the North Atlantic Current, was largely absent.)

[16] Raw bathymetry data are taken from the ETOPO2 2′ topography of *Smith and Sandwell* [1997] and coarsened (by weighted averaging with a cosine-shaped window function) to prevent aliasing errors before interpolation to the model grid. To facilitate exchange at the open Strait of Gibraltar boundary the topography there is manually modified to ensure a minimum sill depth of 300 m. Finally several passes of a smoothing filter reduce the r factor to below 0.2 ($r = \Delta h/2h$) [*Haidvogel and Beckmann*, 1999]. Points where the model grid depth is shallower than 15 m are reset to 15 m.

[17] In the interior of the computational domain we use no explicit horizontal "eddy" viscosity or tracer diffusivity, the model instead relies solely on numerical dissipation from the third-order upstream-biased advection schemes. We apply a linear (quadratic) bottom drag with coefficient $r_D = 3.0 \times 10$ m s^{-4}.

4.2. Forcing and Initial File Preparation

[18] Monthly climatological surface forcing files are created using the tools described by *Penven et al.* [2008],
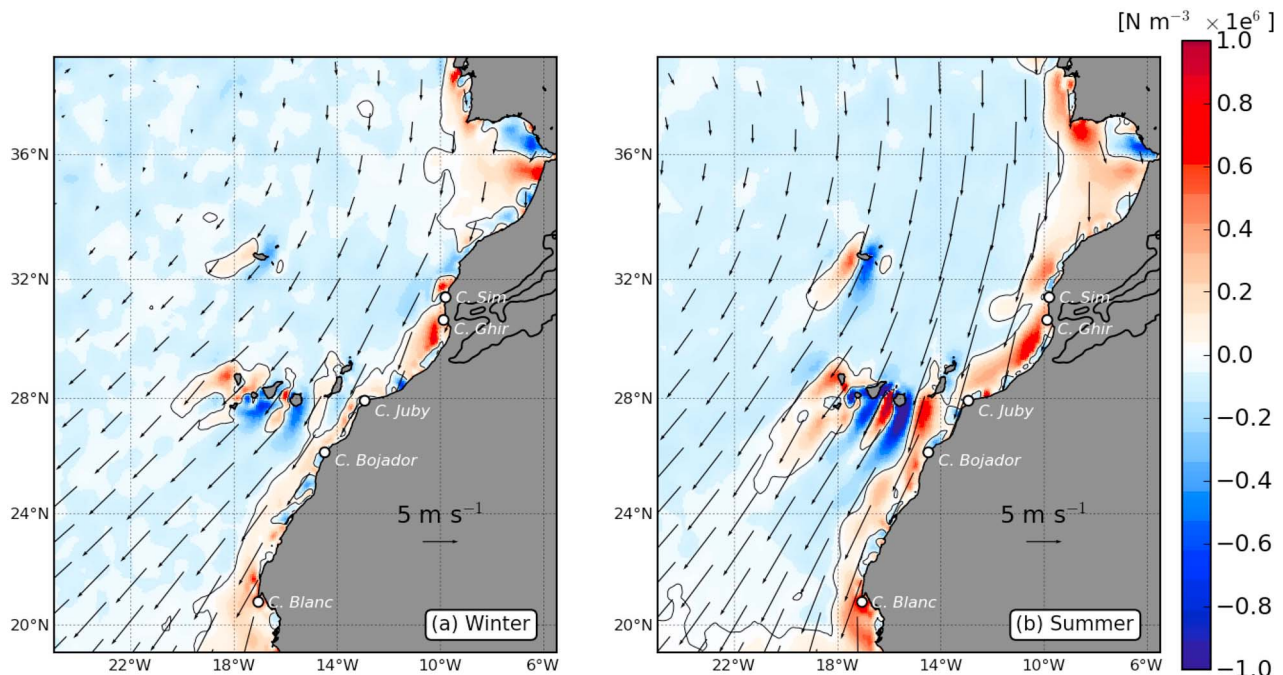
Figure 2. Normalized wind stress curl from the QuikSCAT-derived SCOW wind stress climatology of *Risien and Chelton* [2008] over the northeast Atlantic in (a) winter and (b) summer. Vectors show the wind speed and direction. The zero wind stress curl is contoured in black. Contours over land (1000 and 2000 m) show the Atlas Mountains.

which include heat and freshwater (E-P) fluxes provided by the 1° Comprehensive Ocean-Atmosphere Data Set (COADS) climatology [*Worley et al.*, 2005]. We use a 0.25° surface wind stress product, the 8 year Scatterometer Climatology of Ocean Winds (SCOW, based on QuikSCAT) climatology by *Risien and Chelton* [2008] (see Table 1).

[19] Figure 2 shows fields of the mean SCOW winter and summer wind stress curl along the northwest African coast. There is a general dominance of strong nearshore cyclonic curl, and weak anticyclonic curl offshore [*Bakun and Nelson*, 1991; *Mittelstaedt*, 1991]. The alongshore cyclonic curl has been discussed by *Milliff et al.* [1996], and is an effect of the land–sea temperature contrast: warmer temperatures over northwest Africa set up a persistent continental low-pressure region, which diverts the local anticyclonic atmospheric winds and sets up strong quasi-permanent wind stress curl patterns off the African coast. Intense cyclonic curl in summer off Capes Ghir and Sim may also be related to the influence of the Atlas mountain chain (Figure 2) on the summer Trade winds [*Hagen et al.*, 1996]. Nearshore wind drop off close to the coastal boundary may also be a source of cyclonic curl, but this is most likely absent from the fields in Figure 2 as it is not adequately resolved by the QuikSCAT scatterometer [*Capet et al.*, 2004]. Figures 2a and 2b illustrate the large differences in wind stress curl that occur along the coast over the seasonal cycle.

[20] Thermal forcing at the sea surface is linearized around climatological sea surface temperature (SST; 9.28 km Pathfinder, Table 1) [*Barnier et al.*, 1998]. There is a mild restoration (90 days) of the sea surface salinity (SSS) to climatological values [*Barnier et al.*, 1995]. As northwest

Africa riverine discharges are small [*Warrick and Fong*, 2004] rivers are not included in the configuration.

[21] Lateral boundary forcing and initialization files are prepared using temperature and salinity data from the monthly northeast Atlantic climatology (hereinafter NEAClim) of *Troupin et al.* [2010]. This climatology has a grid resolution of 0.1° and is based on a data set compiled from multiple sources, from which duplicates and outliers are removed. The interpolation technique consists of solving a variational principle that takes into account the misfit between the data and the reconstructed field, and the regularity (or smoothness) of the field. The interpolation is performed using a finite element method which allows for a better resolution of the coastal area. Hence, use of NEAClim (as opposed to lower-resolution climatologies) may be advantageous in nearshore regions, and also to better resolve dynamically important features such as the frontal system associated with the AzC at the western model boundary.

[22] Geostrophic baroclinic velocity components ($\mathbf{u}$) are calculated through the thermal wind relation, where the horizontal velocity at the sea surface ($\mathbf{u}_\zeta$) is the reference velocity. $\mathbf{u}_\zeta$ is obtained through the geostrophic relation, where ζ is first interpolated to the model grid from a monthly sea surface height (SSH) climatology compiled from 15 years of Archiving, Validation, and Interpretation of Satellite Oceanographic data (AVISO) absolute sea level data (see Table 1). An Ekman velocity correction is then applied to $\mathbf{u}$ over a variable depth Ekman layer [*Mason*, 2009]. Barotropic velocities ($\overline{\mathbf{u}}$) are calculated by integrating over h. Finally, a barotropic flux correction is calculated and applied to the velocities in order to enforce volume conservation [*Penven et al.*, 2006; *Mason et al.*, 2010]. The

eastern boundary (Strait of Gibraltar) is treated differently as detailed in section 4.3. All of the variables located at the boundaries are saved to a monthly (2-D) boundary forcing file.

[23] The model is initialized using January values from NEAClim and AVISO, processed similarly to the boundary forcing file so that geostrophic velocities are available as well as tracers.

4.3. Parameterization at the Strait of Gibraltar

[24] The 2 grid cell open boundary at the 300 m deep Strait of Gibraltar is a critical location that controls the exchange between surface outflow of NACW from the Atlantic and, at depth, the Atlantic inflow of dense MW. A parameterization of the prognostic variables in the lateral boundary forcing file enforces the required fluxes which are, approximately, 0.7 Sv (MW, 150–300 m) and 0.8 Sv (NACW, 0–150 m) [*Tsimplis and Bryden*, 2000; *Baschek et al.*, 2001; *Harzallah*, 2009]. Following the methodology laid out by *Peliz et al.* [2007] we use monthly Strait of Gibraltar salinity and temperature profiles from NEAClim for the top layer while, for the bottom layer, temperature and salinity for all months are set as follows: 150+ m (14.23°C, 38.35); 170+ m (13.0°C, 38.5); 200+ m (12.8°C, 38.51); 250+ m (12.6°C, 38.65). A simple algebraic curve gives a u velocity profile appropriate to the required Strait of Gibraltar volume transport. We do not introduce seasonality into the transport. (During development of the configuration we were not aware of any studies of transport variability in the Strait of Gibraltar, however information provided by *Soto-Navarro et al.* [2010] may be useful in future configurations.) The cross-strait velocity, ν, is set to 0 m s^{-1}.

5. Model Validation

[25] In this section a validation of the model solution (hereinafter L0) is performed by comparing instantaneous, mean and eddy variables with observations. This is a common approach to the evaluation of model skill in long-term climatological solutions [*Marchesiello et al.*, 2003; *Penven et al.*, 2005; *Shchepetkin and McWilliams*, 2009]. The 50 year L0 solution reaches equilibrium after ~4 years [*Mason*, 2009]. Averages from the solution are saved every 3 days. Annual and seasonal means are computed using the last 40 years (i.e., years 11–50). The seasons are defined as successive 3 month periods starting from winter defined as months 1–3. The observational data sources and products used throughout the text are summarized in Table 1.

5.1. SST, Surface Velocity, and Thermocline Evolution

[26] The region of the Canary Current System experiences an important seasonal cycle in SST [*Barton et al.*, 1998; *Pelegrí et al.*, 2005a]. Figure 3 compares summer fields of L0 and OSTIA SST (Table 1) in 2 successive years. Also plotted are geostrophic velocity vectors computed from ROMS SSH (η) and merged satellite altimeter data from AVISO (Table 1). Figures 3a–3d are presented primarily to demonstrate the realistic and intrinsic variability achieved within the L0 solution despite our choice of a climatological forcing regime [*Marchesiello et al.*, 2003]. The general distribution of SST in the model agrees rather well with the OSTIA SST. Elevated SST is seen in the Gulf of Cadiz,

along the axis of the AzC at ~34°N, and in the lee of the Canary Islands. Cooler SSTs correspond to upwelling centers along the coasts; the model SST shows a cold bias which is possibly a consequence of uncertainty in the nearshore model wind structure [*Capet et al.*, 2004; *Penven et al.*, 2005]. Upwelling-related filament activity is evident at the major capes, particularly at Cape Ghir [*Pelegrí et al.*, 2005b]. The velocity vectors reveal an abundance of meso-scale meanders and eddies, many of which are clearly associated with the AzC to the north, and with the Canary Islands to the south. Yet these features are ubiquitous outside of these dynamical centers as well. In the region of the CanC a number of coherent structures and recirculations of both signs are visible in the model and observations that channel and modify the mean equatorward flow. The spatial scales of the modeled and observed structures are quite similar.

[27] Long-term means of SST can be a valid diagnostic of model skill. However, because observed SST is used as a correction for the ROMS surface heat fluxes [*Penven et al.*, 2005], such a comparison (i.e., long-term model SST with observed SST) may be misleading. Instead, in Figure 4 we compare monthly means of thermocline temperature from the five Subduction Experiment moorings (SubExp; see Table 1 and labels NW, NE, C, SW, SE on Figure 1) with colocated L0 temperature profiles. The temperature records show a seasonal evolution that penetrates down to about ~100 m in both the moorings and L0. A shallow seasonal thermocline grows in spring and summer, followed by its erosion in autumn and winter. A time delay between the warming of the upper thermocline, which continues to warm after SST has begun to cool, and the surface layers is evident at the central and northern locations. Mixed layer depths (MLD) are also plotted in Figure 4, estimated following the criterion of *de Boyer Montégut et al.* [2004]. MLD spikes in SubExp at NW and NE in April are likely to be caused by the passing of eddies; eddy variability was dominant in the moored velocity records at NE. *Weller et al.* [2004] noted that, contrary to expectation, winter MLD does not shoal significantly to the south in the SubExp records; this behavior is seen also in L0. Deepening of the mixed layer at C and NW is a result of trade-wind-driven Ekman pumping. At SE, the winter MLD is associated with upwelling and shoaling toward the African continent. Mixed layer temperature, however, shows a clearer spatial trend, with the temperature at NW and NE the coldest in winter, and that at SW the warmest for much of the year. Figure 4 demonstrates that the model has a good response to local forcing at the surface, and that spatial and temporal variability of the mixed layer depth is well simulated.

5.2. Mediterranean Water Spreading

[28] A major feature of the thermohaline field of the North Atlantic is the Mediterranean salt tongue [*Richardson et al.*, 1989, 2000]. Figure 5a shows the model annual mean salinity at 1000 m. For comparison, the observed annual mean field from NEAClim is presented in Figure 5b. The NEAClim data show the salty MW signal extending westward away from the Iberian Peninsula, with the largest values for both salinity (and temperature [see *Mason*, 2009]) found just offshore of Cape Roca at 38.8°N (Figure 1). The model salinity anomaly is similar in its zonal distribution at
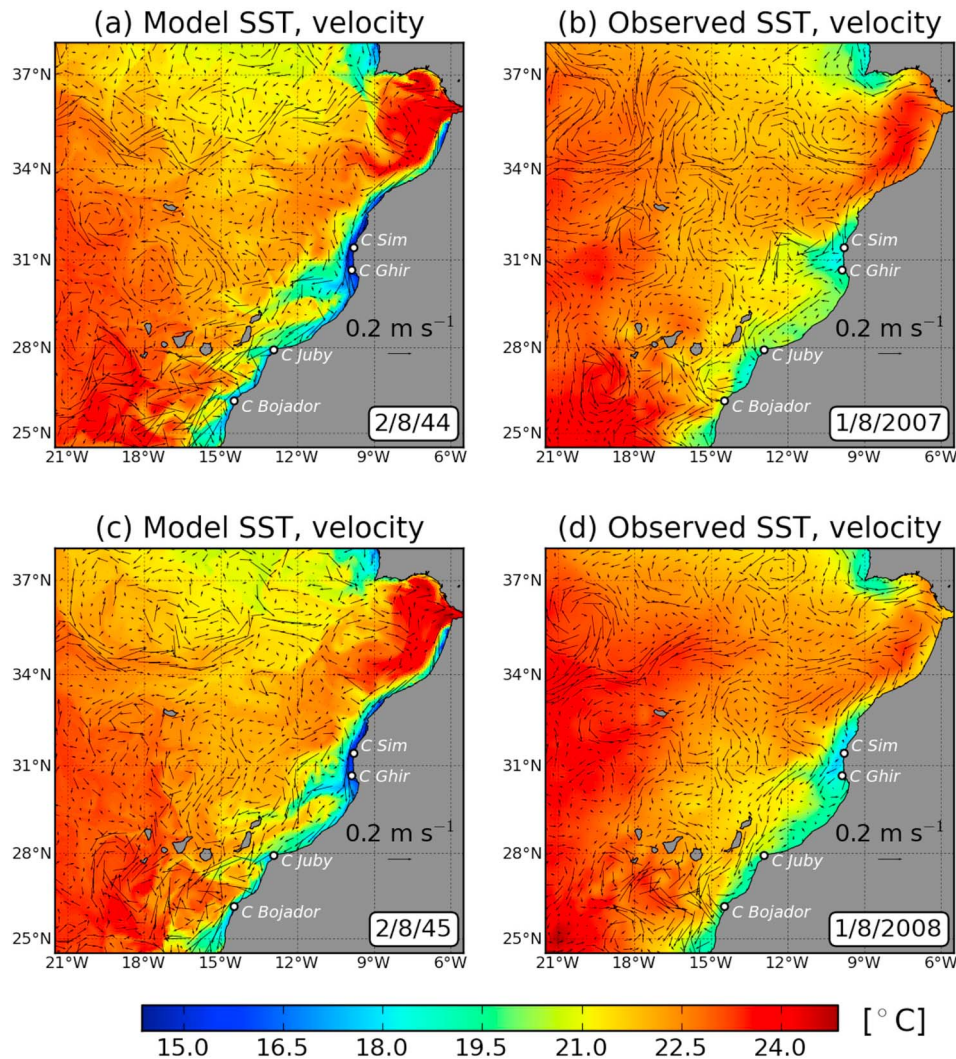
Figure 3. Comparison of SST from L0 (a, c) ROMS and (b, d) OSTIA in two consecutive summers. The L0 (OSTIA) data are 3 day (daily) averages. Vector arrows show nearest contemporaneous surface geostrophic velocities from L0 and from AVISO (AVISO are weekly averages). L0 dates correspond to day/month/year of the solution.

this latitude, although its latitudinal range is rather smaller than the observed anomaly, particularly to the north.

5.3. Zonal Surface Currents

[29] The mean annual distributions of zonal surface currents from L0 (Figure 6a) and from the SVP (Figure 6b) drifter climatology (Table 1) are shown in Figure 6. The SVP velocity field has a generally broad pattern which may be attributed to sampling bias and to the coarse 1° resolution of the data. The zonal components of the NASG stand out. The AzC is visible at ~34°N extending eastward toward the Gulf of Cadiz, its intensity varies but generally decreases along its length. In the southern half of the domain the westward flowing NEC is dominant. The ROMS velocity distribution shows a good qualitative correspondence with the SVP velocities. The large-scale NASG features, i.e., AzC and NEC are evident, though have finer structure than the SVP patterns. The model AzC is strongest between ~19°

and 40°W, similarly to the SVP. Along ~32.5°N there is a zonal counterflow in the model data which is not seen in the drifter data; the Azores CountercCurrent (AzCC) is generally described as being to the north of the AzC [*Alves and Colin de Verdière*, 1999] but there are also reports of its presence to the south [*Pingree*, 1997]. The model NEC does not reproduce the ~0.2 m s⁻¹ velocities seen in the SVP data. This may in part be a result of blocking at the model outflow boundary in the southwest of the domain, which *Mason et al.* [2010] have shown can have an impact on the interior solution.

[30] Strong eastward flows in the northwest of the domain and in the south are associated with the NAC [*Rossby*, 1996] and the NECC [*Lumpkin and Garraffo*, 2005], respectively.

5.4. Sea Surface Height Variance

[31] SSH variance is calculated from the model η fields and compared with SSH observations from AVISO (Table 1).
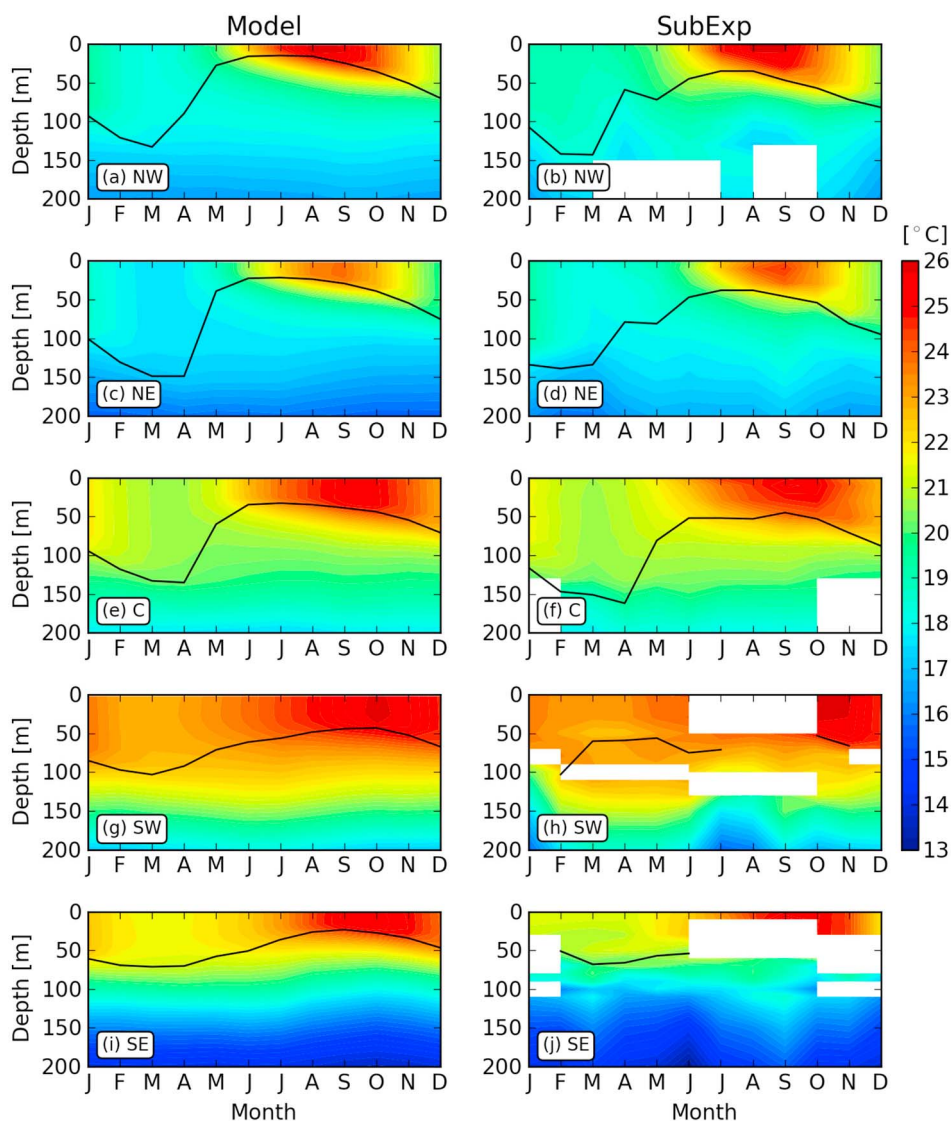
Figure 4. Comparison of monthly mean temperature within the top 200 m from (b, d, f, h, j) the five Subduction Experiment moorings (refer to Figure 1 for the mooring locations) and (a, c, e, g, i) L0. The mixed layer depth is plotted in black. Periods/depths with missing Subduction Experiment data are masked.

Figure 6 shows fields of the annual mean L0 (Figure 6c) and AVISO (Figure 6d) SSH variance. The large-scale distribution of variability is similar in both model and altimetry. High SSH variability is associated with the AzC and the NAC, where baroclinic and barotropic instability is responsible for intense eddy generation [*Le Traon and De Mey*, 1994; *Rossby*, 1996]. The AzC appears as a broader feature than on the zonal velocity plots (Figures 6a and 6b) as a result of meanders and eddy activity along its length. The turbulent NAC occupies much of the northwestern quarter of the domain [*Colin de Verdière et al.*, 1989; *Müller and Siedler*, 1992]; its eastern extent is constrained by the MAR [*Bower et al.*, 2002]. Increased variability is also seen in the lee of the Canary Islands where topography-current interaction produces an energetic eddy field [*Arístegui et al.*, 1994; *Sangrà et al.*, 2009]. Both the CanC and the NEC have relatively weak variability, in agreement with other studies [*Smith et al.*, 2000; *Zhou et al.*, 2000].

[32] In general, the variability of the major currents and structures in the model is lower than the observations, particularly for the AzC. Also, in the region off Cape Ghir it is surprising that the model variability is marginally lower than that of the observations, as it has been shown that the model upwelling here is too strong (section 5.1); this would be expected to lead to greater baroclinic instability at the upwelling front. We suggest that these differences may be a consequence of the use of a temporally smooth monthly climatological wind stress to force the model.

6. Model Canary Current

[33] In section 5.4 the model solution has been shown to give a good representation of the mean and eddy circulation of the eastern subtropical gyre, of which the CanC is an integral part. We now examine the seasonal variability of the modeled CanC.
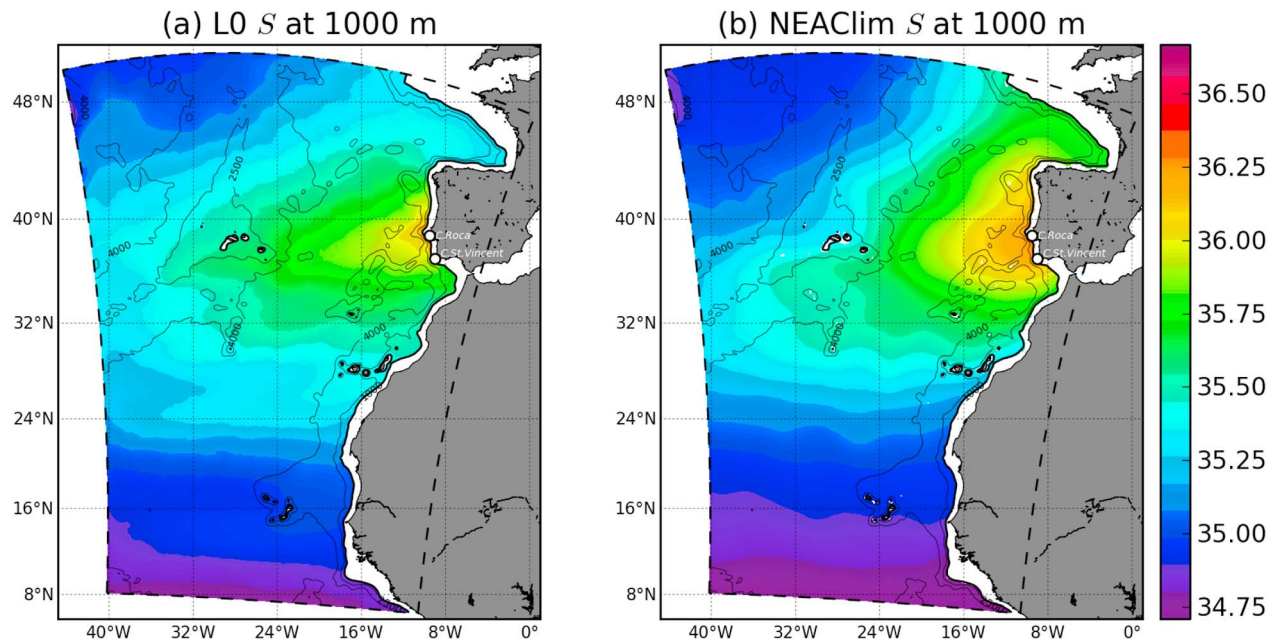
Figure 5. Comparison of annual salinity means at 1000 m from (a) L0 and (b) NEAClim.

6.1. Seasonal Mean Circulation

[34] Seasonal mean fields of the L0 depth-integrated (0–600 m) stream function are shown in Figure 7. The stream function (Ψ) is computed following the procedure outlined by *Penven et al.* [2005] where Ψ is derived from the Laplace equation

$$\nabla^2 \Psi = \nabla \wedge \vec{u}, \qquad (1)$$

with $\nabla \wedge \vec{u}$ the vertical relative vorticity. Solving this equation leads to a representation of the nondivergent part of the horizontal mean currents, i.e., the geostrophic component.

[35] We focus on the region of the CanC in Figure 7 between Madeira, the Canary archipelago, and the African coast and see that, while a net equatorward flux that corresponds to the CanC is evident, the long-term mean circulation displays significant loops and meanders. In winter (Figure 7a) closed streamlines about a local Ψ maximum at ~32°N, 12°W suggest a large coherent anticyclonic flow structure, which we mark A1. In the subsequent seasons (Figures 7b–7d) the position of A1 is seen to track westward across the domain (monthly maps, not shown, confirm this picture). A1 makes small changes in meridional position (~1° southward in autumn) which may be associated with topographic steering near Madeira. A1 appears to originate near to Cape Sim in autumn (marked A1 with a star in Figure 7d) and, after a yearlong passage exits the domain to the west in winter (A1 with a triangle in Figure 7a). The meridional transports associated with A1 along ~32°N are relatively high; if we accept that the southward component of A1 (i.e., the flow at its eastern flank) corresponds to the CanC, then we can conclude that the zonal position of the modeled CanC is mediated by the westward passage of A1.

[36] A1 has a corresponding cyclonic structure at the local Ψ minimum, marked C1, to the south. The two structures are out of phase, with C1 leading A1 by a season. C1 originates south of Cape Ghir in spring (marked C1 with a star in Figure 7b), and leaves the domain over a year later in summer (C1 with a triangle in Figure 7b). C1 has greater meridional variability (between ~29.5° and 30.5°N) than A1, being at its maximum (minimum) in winter (spring/summer). Interaction between C1 and A1 is evident in each season, but is strongest in autumn when it results in intense northwestward flow offshore of Cape Ghir (Figure 7d).

[37] Figures 7a and 7d partially validate the hypothesis of *Pelegrí et al.* [2005a] (see section 2) for an offshore excursion of the nearshore equatorward flow at Cape Ghir and the development of a cyclonic loop around the Canary Islands in winter. The required autumn reversal in the direction of flow along the eastern boundary (i.e., EBC$_{NACW}$; section 3) is present in the model (maximum in November), in good agreement with observations. (We note that while L0 successfully captures the central water reversal, a full examination of the intermediate level behavior is pending [*Mason*, 2009].) However, in the model the loop is closed to the north of the archipelago, rather than the south as proposed by *Pelegrí et al.* [2005a].

6.2. Seasonal Variability at 32°N

[38] Figure 8 shows L0 seasonal sections (0–700 m) of mean meridional velocity across the CanC at 32°N, between the African coast and Madeira. In winter (Figure 8a), a barotropic core of equatorward flow is found at ~11°W (~150 km off the coast). Further to the west at ~13°W there is a strong poleward flow, also barotropic. These flows can be related to A1 in Figure 7a, such that the equatorward component is the wintertime CanC. This pattern can be observed over the subsequent seasons in Figures 8b–8d. In
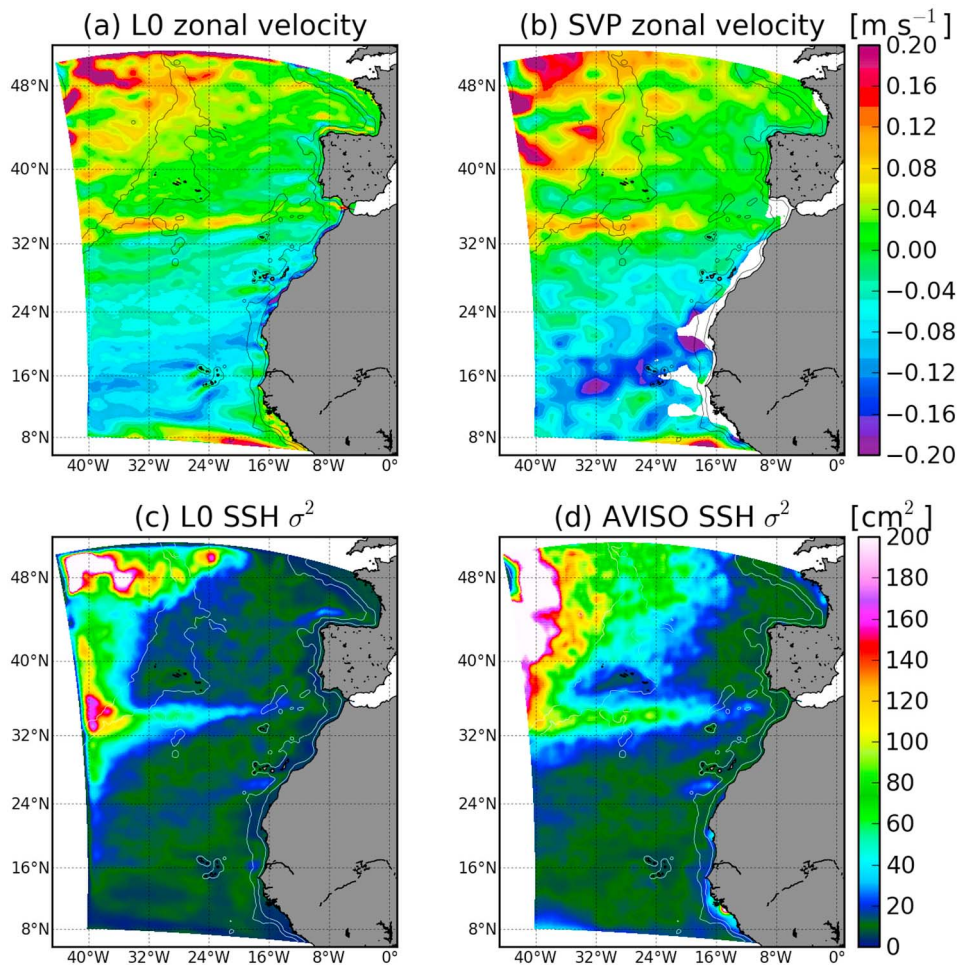
Figure 6. (a, b) Comparison of annual mean zonal velocities from L0 (depth averaged 10–20 m) and from the SVP drifter climatology. The 300 and 3000 m isobaths are plotted in black. SVP regions with less than 100 drifter days per square degree are masked. (c, d) Comparison of annual mean fields of sea surface height variance from L0 and from AVISO. The 300 and 3000 m isobaths are plotted in white.

spring (Figure 8b), strong equatorward flow close to the coast corresponds to the CanUC as the Trade winds begin their seasonal intensification [*Wooster et al.*, 1976; *Pelegrí et al.*, 2006]. By the summertime (Figure 8c), a comparatively broad surface-intensified CanC is centered about 14°W. At the coast, the CanUC is well developed and has an associated poleward undercurrent at depth. The undercurrent is the only poleward flux in the summer section, aside from a shallow surface Ekman layer. Strong equatorward flow at ~16.5°W (weak but present in spring also) is likely related to localized recirculation around Madeira, which forms a barrier to the AzC [*Zhou et al.*, 2000]. Lastly, in autumn (Figure 8d) the CanC is identified at ~16°W. At the coast, the CanUC is replaced by a strong poleward flow centered at around 300 m. Further offshore at ~11.5°W there is a second, weaker, barotropic poleward flow. Figures 8a–8d underline the conclusion for westward migration of the CanC at 32°N in association with the propagation of A1, and demonstrate the vertical extent of the anomaly throughout the central water layer.

[39] Figure 9 compares model seasonal means of accumulated (east to west) barotropic transport at 32°N with the transport derived through the Sverdrup relation [*Sverdrup*, 1942]

$$\bar{v} = \frac{\nabla \wedge \vec{\tau}}{h\beta\rho_0}, \qquad (2)$$

where $\nabla \wedge \vec{\tau}$ is the curl of the seasonal mean SCOW wind stress (Table 1), β is the meridional gradient of the Coriolis parameter (~2.2 × 10^{-11} m^{-1} s^{-1}) and ρ_0 is the model mean seawater density (1027.4 kg m^{-3}). Both the model and Sverdrup transports are meridionally averaged over the latitude range 30.5°–33.5°N. The L0 transports presented are denoted as L0$_{5-15}$, meaning averages computed from L0 years 5–15. Use of L0$_{5-15}$ facilitates comparison with two shorter sensitivity runs (L0$_{NCEP}$ and L0$_{NOMW}$, also shown in Figure 9) which are discussed below in section 7.

[40] For each season the L0$_{5-15}$ transports in Figure 9 converge toward the Sverdrup relation values at ~18°– 19°W indicating that the CanC is largely wind driven over the study region. However there are significant local departures along each transect that suggest that the model circulation experiences additional forcings to the local wind
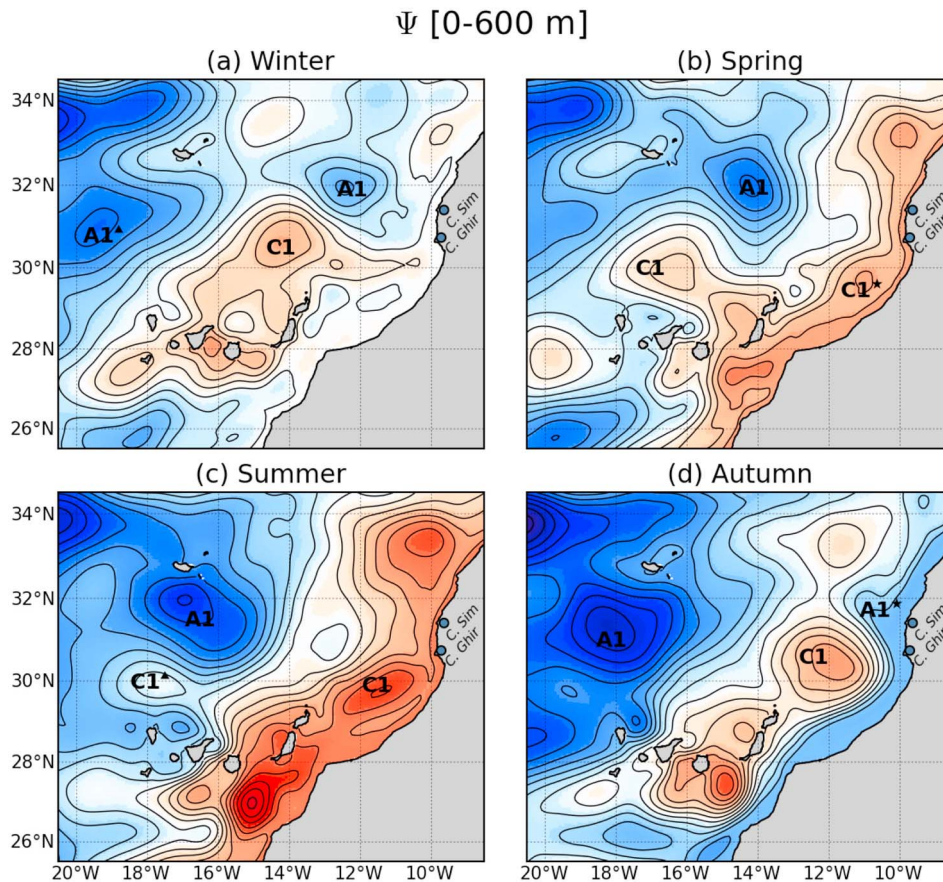
Figure 7. Seasonal mean L0 depth-integrated (0–600 m) stream function (Ψ). Contour intervals are equivalent to 0.5 Sv. Blue (red) shading represents positive (negative) Ψ; flow along positive closed Ψ isolines is clockwise and vice versa. Local maxima (minima) near 32°N (30°N) labeled A1 (C1) mark the passage of an anomalous anticyclonic (cyclonic) mesoscale structure. A1 (C1) with a star indicates the assumed location and season of birth of A1 (C1). A1 (C1) with a triangle shows the position of A1 (C1) from the previous cycle.

forcing. Offshore (west of ~10°W) the positions of these departures are clearly linked to the seasonal propagation of the A1 anomaly. In autumn the effect is amplified by the large-scale poleward flow reversal in the near-shelf region (~10°–12°W) evidenced in Figures 7 and 8.

6.3. Observational Evidence for Modeled Seasonal Variability

[41] It is useful to compare the above model results with available observational evidence. The suggested positions of the CanC as interpreted by *Machín et al.* [2006] from a box model study using in situ data collected at ~32°N during four individual cruises in 1997 and 1998 were shown by red dashed vertical lines in Figure 8. (See Figures 19 and 20 of the observational study by *Machín et al.* [2006]. Figure 19 shows seasonal vertical sections of absolute geostrophic velocity. Figure 20 shows schematic diagrams for each season that give the core position and breadth of the CanC.) The primary important point is that *Machín et al.* [2006] observed a clear westward progression in the position of the observed CanC from spring through autumn (Figures 8b–8d), in accord with our conclusions from the model in sections 6.1

and 6.2. In summer the modeled and observed core positions are identical. In winter, however, *Machín et al.* [2006] place the core in a central position at ~14°W, which is ~250 km further offshore than the winter L0 CanC. They describe the CanC as broad (~280 km) and generally weak. However, an examination of *Machín et al.*'s [2006] vertical section of winter geostrophic velocity (their Figure 19c) reveals a pattern between 100 and 400 km from the coast that is in fact quite similar to the L0 velocity structure shown in Figure 8a. Most importantly, their Figure 19 shows a core of strong southward flow at ~180 km offshore, which coincides rather well with the L0 CanC position identified in Figure 8a at ~11°W.

[42] Table 2 presents mean annual and seasonal equatorward transports of the CanC calculated between 10.5° and 17°W at 32°N. Means from L0 and from the observed transports of *Machín et al.* [2006] are shown. Included also are the 11 year means $L0_{5-15}$, $L0_{NCEP}$ and $L0_{NOMW}$ which are discussed below in section 7. The annual transports are similar for both model and observations. Seasonally, important discrepancies appear to occur in summer and autumn. The model transports are higher in summer, while
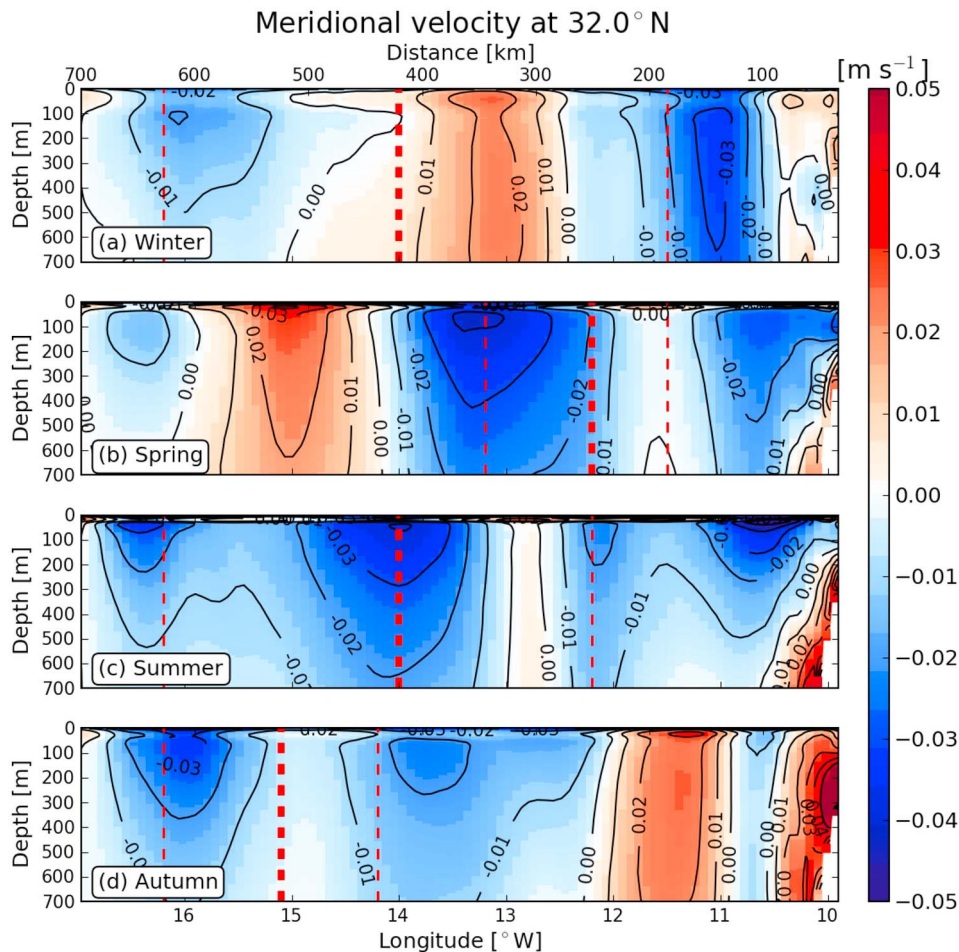
Figure 8. L0 seasonal mean zonal sections of meridional velocity at 32°N. The CanC is visible, particularly in summer where it is centered at ~14°W and reaches 0.05 m s^{-1}. Velocity contours are plotted every 0.01 m s^{-1}, solid (dashed) contours show northward positive (southward negative) velocity. The thick (thin) red dashed lines show the core (outer limits of the) seasonal positions of the CanC as observed by *Machín et al.* [2006].

those of *Machín et al.* [2006] are higher in autumn. We suggest a credible explanation for the apparent discrepancy is that the autumn cruise data used by *Machín et al.* [2006] were collected in September (1997), a summer month in our seasonal means (the L0 mean for September is 5.4 Sv). Considering this fact we conclude that the summer and autumn model transports do correspond well with those of *Machín et al.* [2006].

[43] In Figure 10 we compare mean seasonal sea level anomalies (SLA) from L0 (Figures 10a–10d) and AVISO altimetry (Figures 10e–10h). For the altimetry we use the period 1999–2007, which is the same period as the SCOW wind stress. The modeled and observed SLAs show good agreement in their large-scale magnitudes and distributions, with evidence of a seasonal cycle, upwelling and equatorward flow in summer, and a flow reversal along the coast in autumn. The seasonal cycle can be generalized as a minimum in SSH along the coast during peak upwelling in summer; over the subsequent seasons this minimum propagates offshore. These patterns of seasonal offshore propagation of SSH anomalies have been observed in both

models and altimetry at the California and Peru upwellings and have been linked to wind-generated westward propagating baroclinic planetary waves [*Marchesiello et al.*, 2003; *Penven et al.*, 2005].

[44] The positions of structures A1 and C1 (previously identified in Figure 7) are seen to coincide closely with features (highs and lows) in the model SLAs (Figures 10a–10d). Analogous structures in the altimeter SLA are speculatively labeled A1$_{obs}$ and C1$_{obs}$ in Figures 10e–10h. The correspondence between the modeled and observed SLA anomalies is reasonably good, especially for A1. The closest matches occur in summer and autumn, although in autumn A1 is notably more pronounced than A1$_{obs}$. Between summer and autumn C1$_{obs}$ accelerates away from the coast more rapidly than C1; thereafter the two have similar propagation rates although C1$_{obs}$ leads C1 by ~2°.

6.4. Planetary Waves as a Mechanism for Seasonal Variability

[45] Many reports suggest the presence of westward propagating baroclinic planetary (Rossby) waves within the
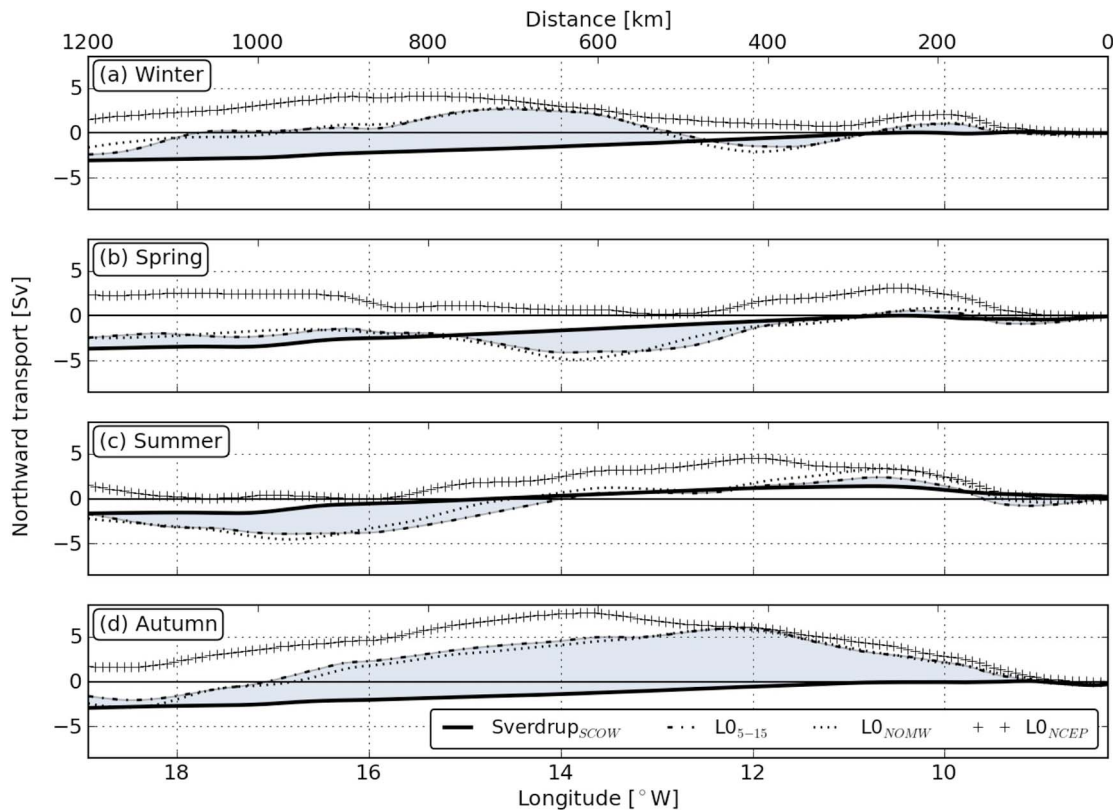
Figure 9. Comparison of seasonal mean accumulated (starting from the eastern boundary) meridional barotropic transports from the model (L0$_{5-15}$, L0$_{NOMW}$, and L0$_{NCEP}$), with the Sverdrup transport derived from the curl of the SCOW wind stress. Grey shading highlights difference between L0$_{5-15}$ and Sverdrup$_{SCOW}$. The transports are meridionally averaged over the latitudes 30.5°–33.5°N.

Canary Basin [*Lippert and Käse*, 1985; *Barnier*, 1988; *Siedler and Finke*, 1993; *Polito and Cornillon*, 1997; *Hagen*, 2001, 2005; *Osychny and Cornillon*, 2004; *Hirschi et al.*, 2007; *Lecointre et al.*, 2008]. (It is argued that the bulk of westward energy propagation at midlatitudes is more representative of nonlinear vertically coherent eddies than of linear Rossby waves [*Chelton et al.*, 2007]; we therefore follow *Lecointre et al.* [2008] in using the term "planetary wave" as a generic descriptor of westward propagating signals.) *Siedler and Finke* [1993] analysed data from a zonal array of five moorings just west of the Canary Islands. They observed annual and semiannual planetary waves with zonal wavelengths of 100–200 and 300 km, respectively. *Hagen* [2005], working with hydrographic data from the open ocean in the Canary Basin, described waves at 32°N with wavelengths of 428 km and periods of 289 days. He showed that waves observed in satellite SLA north of 22°N appear to be seasonally excited. The possibility that westward propagating seasonally forced planetary waves may disturb time mean meridional currents (such as the CanC) is raised by *Hagen* [2001].

[46] Potential instigators of planetary waves exist at the eastern boundary of the Canary Basin, notably temporal variation of the wind stress curl and change of current direction. *Sturges and Hong* [1995] showed a link between wind stress and anomalies in the thermocline depth along 32°N; they showed the spectrum of the (COADS) wind

stress curl to have a peak at 12 months, the intensity generally decreasing from west to east. *Polito and Cornillon* [1997] attributed the generation of midlatitude planetary waves observed through altimetry in the North Atlantic to fluctuations in the wind stress curl at the eastern boundary. *Krauss and Wuebber* [1982] highlighted the dominance of line sources of wind stress along eastern boundaries as planetary wave forcing mechanisms, as opposed to direct wind stress generation. In section 4.2 we noted the significant small-scale variability in the SCOW wind stress curl

Table 2. Mean Annual and Seasonal Equatorward Transports (Sv) in the CanC in the Layer 0–700 m, at 32°N Between 10.5° and 17°W[a]

Solution	Annual	Winter	Spring	Summer	Autumn
L0	3.1	1.5	2.8	5.7	2.5
L0$_{5-15}$	3.0	1.3	3.0	5.3	2.6
L0$_{NCEP}$	1.2	0.1	1.3	2.5	0.9
L0$_{NOMW}$	3.3	1.7	3.4	5.9	2.3
Machín et al. [2006][b]	3.0 ± 1.2	1.7 ± 1.0	2.8 ± 1.2	2.9 ± 1.1	4.5 ± 1.2

[a]Values are shown for the model solutions L0, L0$_{5-15}$, L0$_{NCEP}$, and L0$_{NOMW}$ and from the observational study of *Machín et al.* [2006]. The L0$_{NCEP}$ and L0$_{NOMW}$ solutions are discussed in section 7.
[b]The annual observed values are computed from the four seasonal cruises at 32°N that took place in 1997 and 1998.
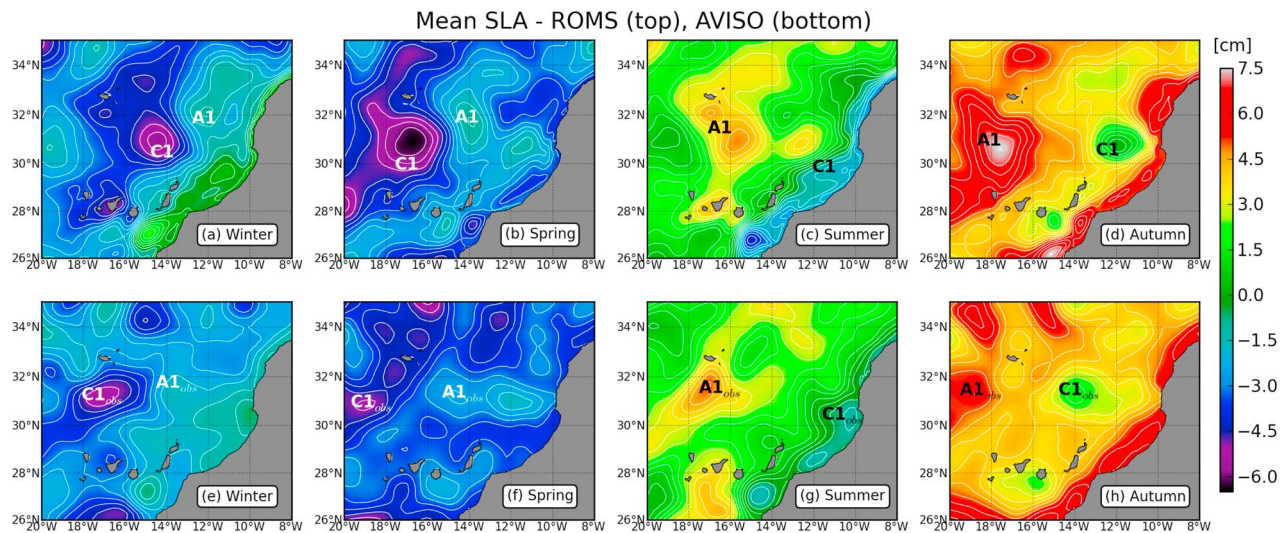
Figure 10. Seasonal mean sea level anomalies. (a–d) The SLAs from L0 and (e–h) the AVISO SLAs (for the same time period as the SCOW wind stress, i.e., 1999–2007) are shown. Contours are plotted in white every 0.5 cm.

encountered along the coast near to Capes Ghir and Sim over the seasonal cycle.

[47] Concerning coastal current reversals, *Mysak* [1983] demonstrated that a fluctuating eastern boundary current can be an efficient generator of annual period baroclinic planetary waves off Vancouver Island in the North Pacific. In section 3 we outlined the annual reversals in the EBC flow that take place along the eastern boundary, and which are captured by the model (Figures 7 and 10). *Siedler and Finke* [1993] observed strong changes in the current near the western Canary Islands, and concluded that, along with wind stress, these were potential candidates for the forcing of the planetary waves they observed at 28°N.

[48] Planetary waves forced at the eastern boundary by combinations of alongshore wind stress fluctuations and equatorially forced Kelvin waves propagating along the coast have been observed in the tropical Atlantic between 4° and 24°N [*Chu et al.*, 2007]. In the present case the influence of Kelvin waves is unlikely as their northward progress is impeded by the frontal regions associated with the northwest African upwelling [*Lazar et al.*, 2006; *Polo et al.*, 2007].

[49] Longitude/time plots (Hovmöler) of monthly mean SSH anomalies and wind stress curl at 32°N (further filtered by meridional averaging between 31.5° and 32.5°N) are presented in Figure 11. Figures 11a and 11b show SSH data from AVISO altimetry and L0, respectively, while Figure 11d shows the SCOW wind stress curl. (Figures 11c and 11e are discussed in section 7.) Three annual cycles are repeated to better illustrate periodicity in the signals. To filter the SSH seasonal cycle we take the difference between each time band and its mean, and then bin the output according to its month, prior to averaging. The largest west–east amplitude difference occurs in summer for both SSH data sets, with the difference being largest in the model; reasons for the divergence in amplitude may include uncertainty in the nearshore structure of the model wind forcing [*Capet et al.*,

2004], interannual variability in the altimeter data, and contamination of the altimeter data close to land [*Ducet et al.*, 2000].
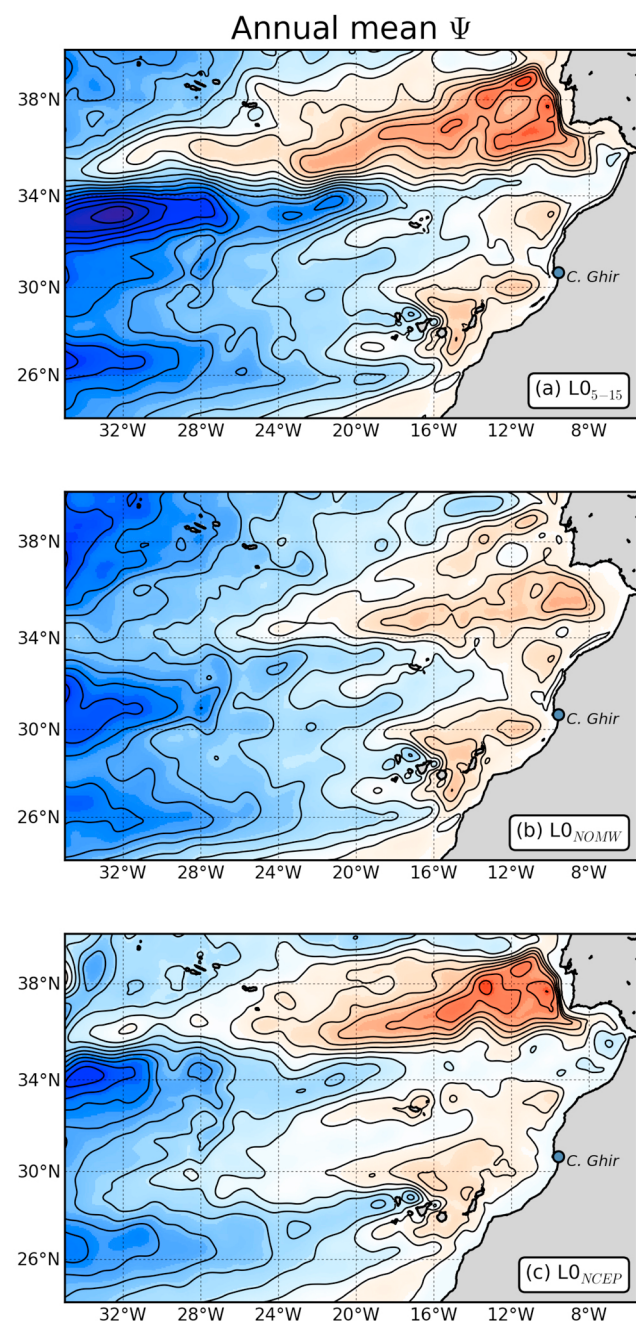
[50] Periodicity at annual time scales is evident in both the observed and modeled SSH anomalies of Figure 11. The cycle for the nearshore wind stress curl is more complex; between early winter and late summer there is generally strong positive curl within 200 km of the shore, with two peaks occurring in late winter and summer. The SSH time series show clear westward propagation of growing positive anomalies, originating in autumn near to the coast and arriving at the western boundary the following summer. This equates to a propagation rate across the domain of ~0.03 m s^{-1}, in good agreement with observations (0.032 m s^{-1}) and theoretical estimates (0.021 m s^{-1}) for the phase speeds of longer-period planetary waves in this region [*Osychny and Cornillon*, 2004; *Hagen*, 2005]. The anomalies correspond to anticyclonic structure A1 shown in Figures 7 and 10. The propagating structure is less well defined in the AVISO data than in L0. Following its autumn generation the AVISO signal is unclear until early winter at ~11–12°W. This behavior can also be observed in Figure 10 above. The autumn generation of the A1 anomaly coincides with a brief transition in the nearshore wind stress curl, which reverses sign for ~3 months in early autumn.

7. Sensitivity Experiments

[51] Two experiments were performed in order to examine the sensitivity of the CanC to upstream variability, and to variability in the large nearshore positive wind stress curl. Annual mean depth-integrated (surface to 7°C isotherm) stream functions calculated from these solutions are shown in Figure 12.

[52] For comparison, Figure 12a shows the stream function from L0$_{5-15}$. The AzC at 34°N is the striking feature in the L0$_{5-15}$ circulation, transporting over 9 Sv at ~21°W. In

Figure 11. Longitude/time plots showing three repeated yearly cycles of monthly mean SSH and wind stress curl at 32°N (meridionally averaged between 31.5° and 32.5°N). SSH is taken from (a) AVISO altimetry, (b) L0, and (c) $L0_{NCEP}$. Contours are shown in black at −0.055, −0.005, and 0.045 m. Years 6–18 (1995–2007) are used from $L0/L0_{NCEP}$ (AVISO). Wind stress curl is taken from (d) SCOW and (e) NCEP. Contours are shown in black every 0.2 N m^{-3} × 1e^6. Intense negative curl in SCOW at the western boundary is associated with Madeira. The seasons are labeled W, S, S, and A for winter, spring, summer, and autumn, respectively.

the Gulf of Cadiz and west of southern Iberia, a large zonal cyclonic recirculation cell loops around Cape St. Vincent before detaching and extending offshore. This cell is related to the topographic β plume of *Kida et al.* [2008], which is a consequence of the geometry of the gulf and entrainment of surface waters into the outflowing MW plume [*Peliz et al.*, 2007]. The cyclonic cell, which may be seen as the AzC (and counterflowing AzCC), has been modeled by *Peliz et al.* [2007] and observations have been reported by *Lamas et al.* [2010]. The AzC in Figure 12a has three southward turning branches at ∼27°, ∼20° and ∼16°W near Madeira, consistent with observations [*Stramma and Siedler*, 1988; *Juliano and Alves*, 2007]. The Madeira branch transports ∼3 Sv as it transitions to the CanC. Off the African coast north and south of Cape Ghir are two large lobes of cyclonic

circulation. The southern lobe is associated with C1, and the region between it and the northern lobe is the location of A1.

7.1. Sensitivity to Azores Current Variability

[53] Given the idea that the AzC feeds the CanC, the question arises as to how sensitive the CanC might be to upstream variability, i.e., changes in the strength of the AzC. It is well established that the AzC in a numerical model can be removed by closing the Strait of Gibraltar [*Jia*, 2000; *Kida et al.*, 2008; *Volkov and Fu*, 2010]. We therefore ran an additional sensitivity experiment (hereinafter $L0_{NOMW}$) using the standard L0 SCOW wind and a closed strait. $L0_{NOMW}$ was run for 15 years, and annual and seasonal means of the prognostic variables were computed using years 5–15.

Figure 12. Comparison of the depth-integrated (surface to 7°C isotherm) annual mean stream function (Ψ) for (a) $L0_{5-15}$, (b) $L0_{NCEP}$, and (c) $L0_{NOMW}$. Contour intervals are equivalent to 1 Sv. Blue (red) shading represents positive (negative) Ψ; flow along positive closed Ψ isolines is clockwise and vice versa.

[54] The effect of the closure of the Strait of Gibraltar upon the AzC can be seen in Figure 12b. The $L0_{NOMW}$ AzC is visible but weak, transporting ~2 Sv at ~21°W, less than a quarter of the $L0_{5-15}$ value. This remnant AzC signal is likely related to the wind [*Townsend et al.*, 2000; *Özgökmen et al.*, 2001]. However, the most interesting aspect of the comparison between the $L0_{5-15}$ and $L0_{NOMW}$ solutions is the southward circulation of the CanC below about 32°N.

Despite the marked differences in the AzC to the north, the twin lobes in $L0_{NOMW}$ between Cape Ghir, Madeira and the Canary Islands are remarkably similar to those in $L0_{5-15}$ in Figure 12a. Table 2 presents $L0_{NOMW}$ annual and seasonal transports across 32°N, these are consistent with but slightly higher than the $L0_{5-15}$ and L0 transports. There is also close agreement between the seasonal accumulated transports from $L0_{NOMW}$ and $L0_{5-15}$ at 32°N in Figure 9. In addition, a plot of the seasonal stream function for $L0_{NOMW}$ (not shown) similar to Figure 7 shows there to be no difference in the positions of anomalies A1 and C1; the anomalies were however slightly more intense, which is in agreement with higher $L0_{NOMW}$ transports across 32°N (Table 2). The results from the $L0_{NOMW}$ experiment suggest that the Canary Current is relatively insensitive to variability in the AzC transport.

7.2. Sensitivity to Wind Stress Curl Variability

[55] To directly examine sensitivity to the wind stress curl we ran an additional numerical experiment forced by monthly mean climatological wind stress derived from 10 m wind speed data at 2.5° resolution from the NCEP Reanalysis Project 1 (see Table 1). The climatological period chosen was 1999–2007 in order to correspond with the SCOW wind stress used for L0. Wind stresses were derived from wind speeds following *Yelland et al.* [1998]. The evolution of the NCEP wind stress curl along 32°N is shown in the longitude/time plot of Figure 11e, where it can be compared with SCOW in the adjacent panel. The NCEP monthly means are markedly smoother than SCOW, although the large-scale structure and seasonal cycle are nominally resolved; a wide band (>1°) of relatively weak cyclonic curl is seen along the coast, and anticyclonic curl over the open ocean. However the (cyclonic) small-scale structure seen in the alongshore SCOW curl is entirely absent. The NCEP-forced simulation, hereinafter $L0_{NCEP}$, was run for 18 years. Annual and seasonal means of the prognostic variables were computed using years 5–15.

[56] Figure 12c shows the $L0_{NCEP}$ annual mean stream function. The circulation is weaker than $L0_{5-15}$. The AzC transports ~6 Sv at ~21°W, and the Madeira branch to the south is absent. The southern lobe of cyclonic flow is missing, while the northern lobe is present but weak. Fields of the $L0_{NCEP}$ seasonal stream function (not shown) have similar large-scale patterns as presented for L0 in Figure 7, but the transports are reduced and there are only hints of the A1 and C1 anomalies.

[57] Figure 11c shows the $L0_{NCEP}$ monthly mean SSH anomaly at 32°N. Small zonal gradients relative to AVISO and L0 (Figures 11a and 11b) confirm an overall weaker circulation. Nevertheless, a weak seasonal cycle persists that is qualitatively comparable to AVISO and L0, and suggestive of a traveling A1 anomaly. Table 2 shows that the $L0_{NCEP}$ seasonal transports are between 53 and 93% smaller than those of L0. Lastly, with reference to the seasonal Sverdrup transport comparisons of Figure 9, the $L0_{NCEP}$ accumulated transports at 32°N are weak and diverge significantly from the Sverdrup and $L0_{5-15}$ transports; this is to be expected given the gross difference in resolution between the SCOW and NCEP wind data. However, the $L0_{NCEP}$ transports do display the local structure identified in Figure 9

for $L0_{5-15}$, and this may be related to the weak traveling anomalies seen in Figure 11c.

[58] Figure 12c indicates that the annual mean circulation (and by extension the seasonal circulation) in the study region is significantly changed with the use of the low-resolution NCEP wind speed product. The largest differences in the structure of the curl between the SCOW and NCEP wind stresses are along the coast. We therefore conclude that small-scale variability in the cyclonic wind stress curl in the vicinity of Cape Ghir (evidenced in Figure 11d) is likely to play an important role in the generation of the A1 and C1 anomalies. However, given the persistence of weak traveling anomalies in $L0_{NCEP}$ seen in Figure 11c, we suggest that a second potential contributor to the formation of the anomalies is the autumn flow reversal of the EBC along the eastern boundary. This phenomenon is less easy to test in a sensitivity experiment using the L0 configuration, as it is more difficult to exclude.

8.   Summary and Conclusions

[59] Results are presented from a high-resolution climatological ocean model simulation for the Canary Basin, using the ROMS ocean model. The focus is on the seasonality of the Canary Current between the latitudes of Madeira and the Canary Island archipelago. The model solution reaches equilibrium after a few years, and thereafter presents no significant drift over its 50 year timespan. A validation exercise, comparing model (instantaneous, seasonal mean and eddy mean) quantities with appropriate observations (from databases, climatologies, and the published literature), shows the model to attain a credible representation of the dynamics of the Canary region: mesoscale variability, mean circulation and the seasonal cycle.

[60] The major currents of the eastern subtropical gyre are well reproduced. The Azores Current is at its correct location, and has levels of mesoscale variability that are comparable with altimeter estimates. The open boundary at the Strait of Gibraltar permits the entrance of dense Mediterranean Water into the model domain; the resulting tracer anomaly spreads at depth into the Atlantic in a realistic manner. Along the eastern boundary the seasonal Canary Upwelling Current jet develops in response to increased upwelling-favorable alongshore wind forcing in spring and summer. The well documented reversal of the large-scale boundary flow (central water levels) takes place in autumn.

[61] From an analysis of the simulated Canary Current circulation we present a novel finding. The seasonal cycle of the CanC in the study region is mediated by the passage of two large-scale coherent anomalous structures that propagate westward following their respective origins near the African coast. Seasonal means of the depth-integrated stream function show an anticyclonic anomaly (A1) that appears north of Cape Ghir in autumn. In spring a cyclonic counterpart (C1) begins to develop south of Cape Ghir. We argue that the core position of the CanC is associated with the equatorward components of these swirling anomalies as they progress westward away from the African coast.

[62] The above result is supported by observational data. The anomalies have a surface expression and are therefore visible to satellite-borne altimeters. Sea level anomaly fields from the model and from altimetry are comparable, the cyclonic and anticyclonic structures show up as respective negative and positive anomalies. The pair are phase locked to the annual cycle and are seen to travel westward at the approximate phase speed of first-mode baroclinic planetary (Rossby) waves at Canary Basin latitudes ($\sim$3 cm s^{-1} or 2.6 km d^{-1}).

[63] Seasonal meridional transports calculated at the latitude of the anticyclone (32°N) are in close agreement with similarly located transports from published in situ observations; the observations include the full extent of the NACW layer and indicate a general westward seasonal progression of the core of the CanC. Plots of seasonal accumulated transport at 32°N computed through the Sverdrup relation confirm that the CanC is largely wind driven. Total model accumulated transports are in agreement with the Sverdrup values. However the model transports show local departures from the Sverdrup transports, and the zonal locations of these departures correspond to that of A1. This reinforces the argument for coastal generation and offshore propagation of A1.

[64] Sensitivity experiments have led to the isolation of two potential candidates for the forcing of the anomalies, namely: (1) small-scale variability in the local wind stress curl at the eastern boundary and (2) major periodic reversals in the flow along the eastern boundary.

[65] In a first experiment to evaluate the role of upstream influence on the CanC by the AzC, we ran a 15 year simulation where the AzC was largely removed (transport reduced by $\sim$85%) by closing the model boundary at the Strait of Gibraltar. We observed minimal impact on the CanC in terms of both its mean position and transport. This result suggests that the CanC is insensitive to variability in the strength of the AzC.

[66] In a second experiment a low-resolution wind stress product was used to force the model. The change from high-resolution wind forcing results in a globally weak circulation; transport by the CanC is reduced by $\sim$60% and the current's mean path, shown by isolines of the stream function, is significantly altered. Nevertheless there is still weak westward propagation of sea level anomalies. We therefore find that nearshore variability in the wind stress curl is important for the dynamics of planetary-wave-like anomalies that significantly influence the path of the CanC between Madeira and the Canary Islands. However, we cannot discount a dynamical contribution from the annual reversal of the large-scale flow along the eastern boundary.

References

Alves, M. L. G. R., and A. Colin de Verdière (1999), Instability dynamics of a subtropical jet and applications to the Azores Front Current System: Eddy-driven mean flow, *J. Phys. Oceanogr.*, 29(5), 837–864, doi:10.1175/1520-0485(1999)029<0837:IDOASJ>2.0.CO;2.

Arhan, M., A. Colin de Verdière, and L. Mémery (1994), The eastern boundary of the subtropical North Atlantic, *J. Phys. Oceanogr.*, 24(6), 1295–1316, doi:10.1175/1520-0485(1994)024<1295:TEBOTS>2.0.CO;2.

Arístegui, J., P. Sangrà, S. Hernández-León, M. Cantón, A. Hernández-Guerra, and J. L. Kerling (1994), Island-induced eddies in the Canary Islands, *Deep Sea Res.*, 49(10), 1087–1101, doi:10.1016/0967-0637(94)90058-2.

Arístegui, J., X. A. Álvarez-Salgado, E. D. Barton, F. G. Figueiras, S. Hernández-León, C. Roy, and A. M. P. Santos (2006), Oceanography and fisheries of the Canary Current/Iberian region of the eastern North Atlantic, in *The Sea: Ideas and Observations on Progress in the Study of the Seas*, vol. 14, pp. 878–931, chap. 23, edited by A. R. Robinson and K. H. Brink, Harvard Univ. Press, Cambridge, Mass.

Arístegui, J., E. D. Barton, X. A. Álvarez-Salgado, A. M. P. Santos, F. G. Figueiras, S. Kifani, S. Hernández-León, E. Mason, and E. Machú (2009), Sub-regional ecosystem variability in the Canary Current upwelling, *Prog. Oceanogr.*, 83(1–4), 33–48, doi:10.1016/j.pocean.2009.07.031.

Bakun, A., and C. S. Nelson (1991), The seasonal cycle of wind-stress curl in subtropical eastern boundary current regions, *J. Phys. Oceanogr.*, 21(12), 1815–1834, doi:10.1175/1520-0485(1991)021<1815:TSCOWS>2.0.CO;2.

Barnier, B. (1988), A numerical study on the influence of the mid-Atlantic Ridge on nonlinear first-mode baroclinic Rossby waves generated by seasonal winds, *J. Phys. Oceanogr.*, 18(3), 417–433.

Barnier, B., L. Siefridt, and P. Marchesiello (1995), Thermal forcing for a global ocean circulation model using a three-year climatology of ECMWF analyses, *J. Mar. Syst.*, 6(4), 363–380, doi:10.1016/0924-7963(94)00034-9.

Barnier, B., P. Marchesiello, A. P. de Miranda, J.-M. Molines, and M. Coulibaly (1998), A sigma-coordinate primitive equation model for studying the circulation in the South Atlantic. Part I: Model configuration with error estimates, *Deep Sea Res.*, 45(4–5), 543–572, doi:10.1016/S0967-0637(97)00086-1.

Barton, E. D. (1987), Meanders, eddies and intrusions in the thermohaline front off northwest Africa, *Oceanol. Acta*, 10(3), 267–283.

Barton, E. D., et al. (1998), The transition zone of the Canary Current upwelling region, *Prog. Oceanogr.*, 41(4), 455–504, doi:10.1016/S0079-6611(98)00023-8.

Baschek, B., U. Send, J. G. Lafuente, and J. Candela (2001), Transport estimates in the Strait of Gibraltar with a tidal inverse model, *J. Geophys. Res.*, 106(C12), 31,033–31,044, doi:10.1029/2000JC000458.

Bower, A. S., B. Le Cann, T. Rossby, W. Zenk, J. Gould, K. Speer, P. L. Richardson, M. D. Prater, and H. M. Zhang (2002), Directly measured mid-depth circulation in the northeastern North Atlantic Ocean, *Nature*, 419, 603–607, doi:10.1038/nature01078.

Brochier, T., E. Mason, M. Moyano, A. Berraho, F. Colas, P. Sangrà, S. Hernández-León, O. Ettahiri, and C. Lett (2011), Ichthyoplankton transport from the African coast to the Canary Islands, *J. Mar. Syst.*, doi:10.1016/j.jmarsys.2011.02.025, in press.

Capet, X. J., P. Marchesiello, and J. C. McWilliams (2004), Upwelling response to coastal wind profiles, *Geophys. Res. Lett.*, 31, L13311, doi:10.1029/2004GL020123.

Chelton, D. B., M. G. Schlax, R. M. Samelson, and R. A. de Szoeke (2007), Global observations of large oceanic eddies, *Geophys. Res. Lett.*, 34, L15606, doi:10.1029/2007GL030812.

Chu, P. C., L. M. Ivanov, O. M. Melnichenko, and N. C. Wells (2007), On long baroclinic Rossby waves in the tropical North Atlantic observed from profiling floats, *J. Geophys. Res.*, 112, C05032, doi:10.1029/2006JC003698.

Colin de Verdière, A., H. Merchier, and M. Arhan (1989), Mesoscale Variability transition from the western to the eastern Atlantic along 48°N, *J. Phys. Oceanogr.*, 19(8), 1149–1170, doi:10.1175/1520-0485(1989)019<1149:MVTFTW>2.0.CO;2.

de Boyer Montégut, C., G. Madec, A. S. Fischer, A. Lazar, and D. Iudicone (2004), Mixed layer depth over the global ocean: An examination of profile data and a profile-based climatology, *J. Geophys. Res.*, 109, C12003, doi:10.1029/2004JC002378.

Ducet, N., P.-Y. Le Traon, and G. Reverdin (2000), Global high-resolution mapping of ocean circulation from TOPEX/Poseidon and ERS-1 and -2, *J. Geophys. Res.*, 105(C8), 19,477–19,498.

Flather, R. A. (1976), A tidal model of the north–west European continental shelf, *Mem. Soc. R. Sci. Liège*, 6(10), 141–164.

Fraile-Nuez, E., and A. Hernández-Guerra (2006), Wind-driven circulation for the eastern North Atlantic Subtropical Gyre from Argo data, *Geophys. Res. Lett.*, 33, L03601, doi:10.1029/2005GL025122.

Fraile-Nuez, E., F. Machín, P. Vélez-Belchí, F. Lóez-Laatzen, R. Borges, V. Benítez-Barrios, and A. Hernández-Guerra (2010), Nine years of mass transport data in the eastern boundary of the North Atlantic Subtropical Gyre, *J. Geophys. Res.*, 115, C09009, doi:10.1029/2010JC006161.

Hagen, E. (2001), Northwest Africa upwelling scenario, *Oceanol. Acta*, 24, suppl. 1, 113–128, doi:10.1016/S0399-1784(00)01110-5.

Hagen, E. (2005), Zonal wavelengths of planetary Rossby waves derived from hydrographic transects in the northeast Atlantic Ocean, *J. Oceanogr.*, 61, 1039–1046, doi:10.1007/s10872-006-0020-3.

Hagen, E., C. Zuelicke, and R. Feistel (1996), Near-surface structures in the Cape Ghir filament off Morocco, *Oceanol. Acta*, 19(6), 577–598.

Haidvogel, D. B., and A. Beckmann (1999), *Numerical Ocean Circulation Modeling*, Imperial Coll. Press, London.

Harzallah, A. (2009), Flow variability in the Strait of Gibraltar: The Mediterranean adjustment to tidal forcing, *Deep Sea Res.*, 56(4), 459–470, doi:10.1016/j.dsr.2008.12.001.

Hernández-Guerra, A., et al. (2002), Temporal variability of mass transport in the Canary Current, *Deep Sea Res.*, 49(17), 3415–3426, doi:10.1016/S0967-0645(02)00092-9.

Hernández-Guerra, A., E. Fraile-Nuez, F. López-Laatzen, A. Martínez, G. Parrilla, and P. Vélez-Belchí (2005), Canary Current and North Equatorial Current from an inverse box model, *J. Geophys. Res.*, 110, C12019, doi:10.1029/2005JC003032.

Hirschi, J. M., P. D. Killworth, and J. R. Blundell (2007), Subannual, seasonal, and interannual variability of the North Atlantic Meridional Overturning Circulation, *J. Phys. Oceanogr.*, 37(5), 1246–1265, doi:10.1175/JPO3049.1.

Jia, Y. (2000), Formation of an Azores Current due to Mediterranean overflow in a modeling study of the North Atlantic, *J. Phys. Oceanogr.*, 30(9), 2342–2358, doi:10.1175/1520-0485(2000)030<2342:FOAACD>2.0.CO;2.

Juliano, M. F., and M. L. G. Alves (2007), The Atlantic subtropical front/current systems of Azores and St. Helena, *J. Phys. Oceanogr.*, 37(11), 2573–2598, doi:10.1175/2007JPO3150.1.

Kalnay, E., et al. (1996), The NCEP/NCAR 40-year reanalysis project, *Bull. Am. Meteorol. Soc.*, 77, 437–471, doi:10.1175/1520-0477(1996)077<0437:TNYRP>2.0.CO;2.

Kida, S., J. F. Price, and J. Yang (2008), The upper oceanic response to overflows: A mechanism for the Azores Current, *J. Phys. Oceanogr.*, 38(4), 880–895, doi:10.1175/2007JPO3750.1.

Kilpatrick, K., G. P. Podesta, and R. Evans (2001), Overview of the NOAA/NASA Advanced Very High Resolution Radiometer Pathfinder algorithm for sea surface temperature and associated matchup database, *J. Geophys. Res.*, 106(C5), 9179–9197.

Knoll, M., A. Hernández-Guerra, B. Lenz, F. López-Laatzen, F. Machín, T. J. Müller, and G. Siedler (2002), The eastern boundary current system between the Canary Islands and the African Coast, *Deep Sea Res.*, 49(17), 3427–3440, doi:10.1016/S0967-0645(02)00105-4.

Krauss, W., and C. Wuebber (1982), Response of the North Atlantic to annual wind variations along the eastern coast, *Deep Sea Res.*, 29(7), 851–868, doi:10.1016/0198-0149(82)90050-4.

Lamas, L., Á. Peliz, I. Ambar, A. B. Aguiar, N. Maximenko, and A. Teles-Machado (2010), Evidence of time-mean cyclonic cell southwest of the Iberian Peninsula: The Mediterranean outflow-driven β-plume?, *Geophys. Res. Lett.*, 37, L12606, doi:10.1029/2010GL043339.

Large, W. G., J. C. McWilliams, and S. C. Doney (1994), Oceanic vertical mixing: A review and a model with a vertical K-profile boundary layer parameterization, *Rev. Geophys.*, 32(4), 363–403.

Lathuiliére, C., V. Echevin, and M. Lévy (2008), Seasonal and intraseasonal surface chlorophyll-a variability along the northwest African coast, *J. Geophys. Res.*, 113, C05007, doi:10.1029/2007JC004433.

Lazar, A., I. Polo, S. Arnault, and G. Mainsant (2006), Kelvin wave activity in the eastern tropical Atlantic, paper presented at 15 Years of Progress in Radar Altimetry Symposium, Eur. Space Agency, Venice, Italy.

Lecointre, A., T. Penduff, P. Cipollini, R. Tailleux, and B. Barnier (2008), Depth dependence of westward-propagating North Atlantic features diagnosed from altimetry and a numerical 1/6° model, *Ocean Sci.*, 4, 99–113.

Le Traon, P.-Y., and P. De Mey (1994), The eddy field associated with the Azores Front east of the Mid-Atlantic Ridge as observed by the Geosat altimeter, *J. Geophys. Res.*, 99(C5), 9907–9924, doi:10.1029/93JC03513.

Lippert, A., and R. H. Käse (1985), Stochastic wind forcing of baroclinic Rossby waves in the presence of a meridional boundary, *J. Phys. Oceanogr.*, 15(2), 184–194, doi:10.1175/1520-0485(1985)015<0184:SWFOBR>2.0.CO;2.

Lumpkin, R., and Z. Garraffo (2005), Evaluating the decomposition of tropical Atlantic drifter observations, *J. Atmos. Oceanic Technol.*, 22(9), 1403–1415, doi:10.1175/JTECH1793.1.

Machín, F., and J. L. Pelegrí (2009), Northward penetration of Antarctic Intermediate Water off northwest Africa, *J. Phys. Oceanogr.*, 39(3), 512–535, doi:10.1175/2008JPO3825.1.

Machín, F., A. Hernández-Guerra, and J. L. Pelegrí (2006), Mass fluxes in the Canary Basin, *Prog. Oceanogr.*, 70(2–4), 416–447.

Machín, F., J. L. Pelegrí, E. Fraile-Nuez, P. Vélez-Belchí, F. Lóez-Laatzen, and A. Hernández-Guerra (2010), Seasonal flow reversals of intermediate waters in the Canary Current System east of the Canary Islands, *J. Phys. Oceanogr.*, 40(8), 1902–1909, doi:10.1175/2010JPO4320.1.

Marchesiello, P., J. C. McWilliams, and A. F. Shchepetkin (2003), Equilibrium structure and dynamics of the California Current System, *J. Phys. Oceanogr.*, 33(4), 753–783, doi:10.1175/1520-0485(2003)33<753:ESADOT>2.0.CO;2.

Mason, E. (2009), High-resolution modelling of the Canary Basin oceanic circulation, Ph.D. thesis, 235 pp., Univ. de Las Palmas de Gran Canaria, Las Palmas de Gran Canaria, Spain.

Mason, E., J. Molemaker, F. Colas, A. F. Shchepetkin, J. C. McWilliams, and P. Sangrà (2010), Procedures for offline grid nesting in regional ocean models, *Ocean Modell.*, 35(1–2), 1–15, doi:10.1016/j.ocemod.2010.05.007.

Milliff, R. D., W. G. Large, W. R. Holland, and J. C. McWilliams (1996), The General circulation responses of high-resolution North Atlantic Ocean models to synthetic scatterometer winds, *J. Phys. Oceanogr.*, 26(9), 1747–1768.

Mittelstaedt, E. (1991), The ocean boundary along the northwest African coast: Circulation and oceanographic properties at the sea surface, *Prog. Oceanogr.*, 26(4), 307–355, doi:10.1016/0079-6611(91)90011-A.

Müller, T. J., and G. Siedler (1992), Multi-year current time series in the eastern North Atlantic Ocean, *J. Mar. Res.*, 50, 63–98.

Mysak, L. A. (1983), Generation of annual Rossby waves in the North Pacific, *J. Phys. Oceanogr.*, 13(10), 1908–1923.

Navarro-Pérez, E., and E. D. Barton (2001), Seasonal and interannual variability of the Canary Current, *Sci. Mar.*, 65, suppl. 1, 205–213.

Osychny, V., and P. Cornillon (2004), Properties of Rossby waves in the North Atlantic estimated from satellite data, *J. Phys. Oceanogr.*, 34(1), 61–76, doi:10.1175/1520-0485(2004)034<0061:PORWIT>2.0.CO;2.

Özgökmen, T. M., E. P. Chassignet, and C. G. H. Rooth (2001), On the Connection between the Mediterranean outflow and the Azores Current, *J. Phys. Oceanogr.*, 31(2), 461–480, doi:10.1175/1520-0485(2001)031<0461:OTCBTM>2.0.CO;2.

Pascual, A., Y. Faugère, G. Larnicol, and P.-Y. Le Traon (2006), Improved description of the ocean mesoscale variability by combining four satellite altimeters, *Geophys. Res. Lett.*, 33, L02611, doi:10.1029/2005GL024633.

Pelegrí, J. L., et al. (2005a), Coupling between the open ocean and the coastal upwelling region off northwest Africa: Water recirculation and offshore pumping of organic matter, *J. Mar. Syst.*, 54(1–4), 3–37, doi:10.1016/j.jmarsys.2004.07.003.

Pelegrí, J. L., et al. (2005b), Hydrographic cruises off northwest Africa: The Canary Current and the Cape Ghir region, *J. Mar. Syst.*, 54(1–4), 39–63, doi:10.1016/j.jmarsys.2004.07.001.

Pelegrí, J. L., A. Marrero-Díaz, and A. W. Ratsimandresy (2006), Nutrient irrigation of the North Atlantic, *Prog. Oceanogr.*, 70(2–4), 366–406, doi:10.1016/j.pocean.2006.03.018.

Peliz, Á. J., J. Dubert, P. Marchesiello, and A. Teles-Machado (2007), Circulation in the Gulf of Cadiz: Model and mean flow structure, *J. Geophys. Res.*, 112, C11015, doi:10.1029/2007JC004159.

Penven, P., V. Echevin, J. Pasapera, F. Colas, and J. Tam (2005), Average circulation, seasonal cycle, and mesoscale dynamics of the Peru Current System: A modeling approach, *J. Geophys. Res.*, 110, C10021, doi:10.1029/2005JC002945.

Penven, P., L. Debreu, P. Marchesiello, and J. C. McWilliams (2006), Evaluation and application of the ROMS 1-way embedding procedure to the central California upwelling system, *Ocean Modell.*, 12(1–2), 157–187, doi:10.1016/j.ocemod.2005.05.002.

Penven, P., P. Marchesiello, L. Debreu, and J. Lefevre (2008), Software tools for pre- and post-processing of oceanic regional simulations, *Environ. Model. Software*, 23(5), 660–662, doi:10.1016/j.envsoft.2007.07.004.

Pingree, R. D. (1997), The Eastern Subtropical Gyre (North Atlantic): Flow rings recirculations structure and subduction, *J. Mar. Biol. Assoc. U. K.*, 77(3), 573–624, doi:10.1017/S0025315400036109.

Polito, P. S., and P. Cornillon (1997), Long baroclinic Rossby waves detected by TOPEX/POSEIDON, *J. Geophys. Res.*, 102(C2), 3215–3235, doi:10.1029/96JC03349.

Polo, I., A. Lazar, B. Rodriguez-Fonseca, and S. Arnault (2007), Oceanic Kelvin waves and tropical Atlantic intraseasonal variability: 1. Kelvin wave characterization, *J. Geophys. Res.*, 113, C07009, doi:10.1029/2007JC004495.

Richardson, P. L., J. F. Price, D. Walsh, L. Armi, and M. Schröder (1989), Tracking three meddies with SOFAR floats, *J. Phys. Oceanogr.*, 19(3), 371–383, doi:10.1175/1520-0485(1989)019<0371:TTMWSF>2.0.CO;2.

Richardson, P. L., A. S. Bower, and W. Zenk (2000), A census of Meddies tracked by floats, *Prog. Oceanogr.*, 45(2), 209–250, doi:10.1016/S0079-6611(99)00053-1.

Rio, M.-H., and F. Hernández (2004), A mean dynamic topography computed over the world ocean from altimetry, in situ measurements and a geoid model, *J. Geophys. Res.*, 109, C12032, doi:10.1029/2003JC002226.

Risien, C. M., and D. B. Chelton (2008), A global climatology of surface wind and wind stress fields from eight years of QuikSCAT scatterometer data, *J. Phys. Oceanogr.*, 38(11), 2379–2413, doi:10.1175/2008JPO3881.1.

Rossby, T. (1996), The North Atlantic Current and surrounding waters: At the crossroads, *Rev. Geophys.*, 34(4), 463–481.

Sangrà, P., et al. (2009), The Canary Eddy Corridor: A major pathway for long-lived eddies in the subtropical North Atlantic, *Deep Sea Res.*, 56, 2100–2114, doi:10.1016/j.dsr.2009.08.008.

Shchepetkin, A. F., and J. C. McWilliams (2005), The Regional Oceanic Modeling System (ROMS): A split-explicit, free-surface, topography-following-coordinate oceanic model, *Ocean Modell.*, 9(4), 347–404, doi:10.1016/j.ocemod.2004.08.002.

Shchepetkin, A. F., and J. C. McWilliams (2009), Correction and commentary for "Ocean forecasting in terrain-following coordinates: Formulation and skill assessment of the Regional Ocean Modeling System" by Haidvogel et al., J. Comp. Phys. 227, pp. 3595–3624, *J. Comput. Phys.*, 228(24), 8985–9000, doi:10.1016/j.jcp.2009.09.002.

Siedler, G., and M. Finke (1993), Long-period transport changes in the eastern North Atlantic and their simulation by propagating waves, *J. Geophys. Res.*, 98(C2), 2393–2406, doi:10.1029/92JC02122.

Smith, R. D., M. E. Maltrud, F. O. Bryan, and M. W. Hecht (2000), Numerical simulation of the North Atlantic Ocean at 1/10°, *J. Phys. Oceanogr.*, 30(7), 1532–1561, doi:10.1175/1520-0485(2000)030<1532:NSOTNA>2.0.CO;2.

Smith, W. H. F., and D. T. Sandwell (1997), Global sea floor topography from satellite altimetry and ship depth soundings, *Science*, 277(5334), 1956–1962, doi:10.1126/science.277.5334.1956.

Soto-Navarro, J., F. Criado-Aldeanueva, J. García-Lafuente, and A. Sánchez-Román (2010), Estimation of the Atlantic inflow through the Strait of Gibraltar from climatological and in situ data, *J. Geophys. Res.*, 115, C10023, doi:10.1029/2010JC006302.

Spall, M. A. (1990), Circulation in the Canary Basin: A model/data analysis, *J. Geophys. Res.*, 95(C6), 9611–9628.

Stark, J. D., C. J. Donlon, M. J. Martin, and M. E. McCulloch (2007), OSTIA: An operational, high resolution, real time, global sea surface temperature analysis system, in *OCEANS 2007—Europe*, pp. 1–4, doi:10.1109/OCEANSE.2007.4302251, Inst. of Electr. and Electr. Eng., Piscataway, N. J.

Stramma, L. (1984), Geostrophic transport in the warm water sphere of the eastern subtropical North Atlantic, *J. Mar. Res.*, 42, 537–558.

Stramma, L., and G. Siedler (1988), Seasonal changes in the North Atlantic Subtropical Gyre, *J. Geophys. Res.*, 93(C7), 8111–8118.

Sturges, W., and B. G. Hong (1995), Wind forcing of the Atlantic thermocline along 32°N at low frequencies, *J. Phys. Oceanogr.*, 25(7), 1706–1715, doi:10.1175/1520-0485(1995)025<1706:WFOTAT>2.0.CO;2.

Sverdrup, H. U. (1942), Wind-driven currents in a baroclinic ocean; with application to the equatorial currents of the eastern Pacific, *Proc. Natl. Acad. Sci. U. S. A.*, 33, 318–326.

Townsend, T. L., H. E. Hurlburt, and P. J. Hogan (2000), Modeled Sverdrup flow in the North Atlantic from 11 different wind stress climatologies, *Dyn. Atmos. Oceans*, 32(3–4), 373–417, doi:10.1016/S0377-0265(00)00052-X.

Troupin, C., F. Machín, M. Ouberdous, D. Sirjacobs, A. Barth, and J.-M. Beckers (2010), High-resolution climatology of the northeast Atlantic using Data-Interpolating Variational Analysis (DIVA), *J. Geophys. Res.*, 115, C08005, doi:10.1029/2009JC005512.

Tsimplis, M. N., and H. L. Bryden (2000), Estimation of the transports through the Strait of Gibraltar, *Deep Sea Res.*, 47(12), 2219–2242, doi:10.1016/S0967-0637(00)00024-8.

Volkov, D. L., and L.-L. Fu (2010), On the reasons for the formation and variability of the Azores Current, *J. Phys. Oceanogr.*, 40(10), 2197–2220, doi:10.1175/2010JPO4326.1.

Warrick, J. A., and D. A. Fong (2004), Dispersal scaling from the world's rivers, *Geophys. Res. Lett.*, 31, L04301, doi:10.1029/2003GL019114.

Weller, R. A., M. A. Furey, P. W. Spall, and R. E. Davis (2004), The large-scale context for oceanic subduction in the Northeast Atlantic, *Deep Sea Res.*, *51*(5), 665–699, doi:10.1016/j.dsr.2004.01.003.

Wooster, W. S., A. Bakun, and D. R. McLain (1976), The seasonal upwelling cycle along the eastern boundary of the North Atlantic, *J. Mar. Res.*, *34*, 131–140.

Worley, S. J., S. D. Woodruff, R. W. Reynolds, S. J. Lubker, and N. Lott (2005), ICOADS release 2.1 data and products, *Int. J. Climatol.*, *25*(7), 823–842, doi:10.1002/joc.1166.

Yelland, M. J., B. I. Moat, P. K. Taylor, R. W. Pascal, J. Hutchings, and V. C. Cornell (1998), Wind stress measurements from the open ocean corrected for airflow distortion by the ship, *J. Phys. Oceanogr.*, *28*(7), 1511–1526, doi:10.1175/1520-0485(1998)028<1511:WSMFTO>2.0.CO;2.

Zenk, W., B. Klein, and M. Schröder (1991), Cape Verde frontal zone, *Deep Sea Res.*, *38*(S1), 505–530.

Zhou, M., J. D. Paduan, and P. P. Niiler (2000), Surface currents in the Canary Basin from drifter observations, *J. Geophys. Res.*, *105*(C9), 21,893–21,911.

F. Colas, J. C. McWilliams, J. Molemaker, and A. F. Shchepetkin, Institute of Geophysics and Planetary Physics, University of California, 3637 Geology Bldg., 405 Hilgard Ave., Los Angeles, CA 90095-1567, USA.

E. Mason, Departament d'Oceanografía Física, Institut de Ciències del Mar, CMIMA-CSIC, Passeig Marítim de la Barceloneta 37-49, E-08003 Barcelona, Spain. (emason@icm.csic.es)

P. Sangrà, Departamento de Física, Universidad de Las Palmas de Gran Canaria, Campus de Tafira, E-35017 Las Palmas de Gran Canaria, Spain.

C. Troupin, GeoHydrodynamics and Environment Research, Universitè de Liège, Allée du 6 Août 17, Sart Tilman B5a, B-4000 Liège 1, Belgium.